Alma Mater Studiorum · Università di Bologna

Department of Physics and Astronomy "Augusto Righi"
Degree Course in Physics

Effects of Deglaciation on Topography in North America

Supervisor:
Prof. Giorgio Spada

Submitted by:
Federica Naldi

Academic Year 2024/2025

Sommario

Lo scopo di questa indagine è quello di analizzare l'evoluzione temporale e i parametri di controllo del rigonfiamento post-glaciale, una struttura sopraelevata che si forma ai lati di un ghiacciaio come risposta isostatica alla presenza del carico. Per farlo, sono stati utilizzati gli spostamenti radiali e i tassi di spostamento radiale ottenuti con le simulazioni numeriche del programma TABOO, che ha permesso di valutare anche il contributo dell'isostasia glaciale all'aumento del livello marino dal 1850 ad oggi; per farlo, il minimo tasso di subsidenza attuale calcolato da TABOO è stato confrontato con il trend annuale ((2.90 $\pm$ 0.12) mm/yr) proveniente dai dati mareografici della stazione The Battery a New York (40.7°N, 74°W), e successivamente corretto tenendo conto di effetti attuali dovuti al cambiamento climatico e allo scioglimento dei ghiacciai ((1.3 $\pm$ 0.7) mm/yr).
In particolare, le simulazioni mostrano che il rigonfiamento post-glaciale continua a crescere durante lo scioglimento della calotta glaciale; raggiunta la massima ampiezza, inizia a muoversi verso l'interno mentre collassa, per poi invertire il suo moto orizzontale e migrare verso l'esterno. Per il presente, le simulazioni di TABOO prevedono un tasso di subsidenza annuale di -3.3 mm/yr, un valore non compatibile con i dati mareografici della stazione di New York The Battery.
Infine, per quanto riguarda la forma e i tassi di subsidenza del rigonfiamento, è stato possibile determinare che la prima dipende principalmente dallo spessore della litosfera e dalla viscosità dello strato più alto del mantello. Inoltre, sono state trovate delle differenze significative nell'ampiezza del rigonfiamento rimuovendo la condizione di equilibrio all'ultimo massimo glaciale. Invece, per quanto riguarda i tassi di subsidenza, le maggiori variazioni sono state rilevate modificando la durata di formazione del carico, la sua semiampiezza angolare, lo spessore litosferico e la viscosità degli strati del mantello.

Abstract

The purpose of this investigation is to analyze the temporal evolution and the controlling factors of the galcial forebulge, which is an isostatic upheaval induced by a glacial load. In order to do so, radial displacements and the corresponding rates were taken into account. The evolution of these physical quantities was determined by numerical simulations performed by TABOO program, which was also used to determine the contribution of glacial isostasy to the Rising Sea Level (RSL) from 1850s to nowadays; therefore, TABOO's results were compared with the annual trend ((2.90 $\pm$ 0.12) mm/yr) obtained from tide gauge records measured at New York The Battery station (40.7°N, 74°W), corrected by taking into consideration current climate change effects and ice melting ((1.3 $\pm$ 0.7) mm/yr).

In particular, the results of the simulations show that the postglacial forebulge keeps forming while the load is melting; after reaching its maximum amplitude, it starts moving inward and collapsing; in the end, the forebulge will invert its horizontal motion and start migrating outwards. As of today, TABOO predictions establish a minimum annual rate of subsidence of -3.3 mm/yr. However, this value is not compatible with tide gauge data from New York The Battery station, as it overestimates the contribution to rising sea level of post-glacial isostasy.

In the end, it was possible to establish that the forebulge shape depends mainly on the lithosphere thickness and on the viscosity of the topmost mantle layer; furthermore, significant differences on the forebulge shape were found by removing the condition of isostatic equilibrium at the Last Glacial Maximum. On the other hand, significant changes in rates of radial displacement were found by varying the duration of the load formation, the load angular half amplitude, and both the lithospheric thickness and the viscosity of all mantle layers.

Contents

Sommario **1**

Abstract **2**

1 Introduction to the Surface Loading Problem **4**
1.1 Surface Loads 5
1.2 The Viscoelastic Model 6
1.3 Response to Surface Loads 6
1.4 Response to AX Loads 8

2 Method **13**
2.1 Model 13
2.2 Forebulge Time Evolution 16
2.3 Current Land Subsidence and Rising Sea Level 17
2.4 Controlling Parameters of the Forebulge 19

3 Results **23**
3.1 Forebulge Time Evolution 23
3.2 Current Land Subsidence and Rising Sea Level 28
3.3 Controlling Parameters of the Forebulge 30

Conclusions **40**

References **42**

Ringraziamenti **44**

1. Introduction to the Surface Loading Problem

A peripheral bulge, also known as forebulge, is formed as an isostatic response to a glacial load which acts upon the lithosphere long enough to cause its flexure. As a consequence, a bulge takes shape outside the region covered by the load so that isostatic equilibrium is reached, since the bending of the lithosphere causes a flow of mantle materials that accumulate at the margins of the load. This investigation aims at shedding light on the dynamics of this process, since the bulge starts collapsing and migrating after reaching its maximum amplitude. These deformations of the lithosphere can have crucial consequences on Rising Sea Level (RSL) in coastal cities which now stand on the forebulge. Therefore, it is fundamental to be able to predict the extent to which the forebulge collapse can affect the RSL in these regions [Brandes et al., 2025].
This study was made possible by the use of TABOO [1], a post-glacial rebound calculator. In fact, TABOO allows for the simulation of the Earth's response to various loads with different time histories. In particular, the program is based on the following assumptions on the Earth [Spada, 2003b]:

1. It is Spherically symmetric (TABOO solves 1D problems), Viscoelastic, Incompressible and Self-Gravitating (SVISG model);

2. it is non-rotating.

An analytical expression for the displacements induced by a surface load can be found by solving the equilibrium equations for a SVISG Earth. Therefore, before deriving the analytical model for the Earth response, it is necessary to introduce the mathematical model for surface loads and for viscoelasticity. In particular, the following treatise is based on Spada and Melini's book "Glacial Isostatic Adjustment: Theory for a Spherically Symmetric Earth and Numerical Results" [Spada and Melini, 2025] and on Spada's work "The theory behind TABOO" [Spada, 2003b].

[1] TABOO (Spada 2003) is available from https://github.com/danielemelini/TABOO. It was originally distributed by the Samizdat Press and now it can also be found at the page https://samizdat.mines.edu/.

1.1 Surface Loads

The surface loads that generate the perturbation can be of two kinds: axis-symmetric (AX loads), if they have axial simmetry, or non axis-symmetric (NAX loads), if not. Clearly, AX loads can be treated as a sub-case of NAX loads.
The surface load is defined as follows:

$$L(t,\theta,\lambda) = -\frac{1}{\gamma_0}\frac{df_n}{dA}(t,\theta,\lambda) \tag{1.1}$$

where df_n is the normal force acting on the Earth's surface $dA = a^2 d\Omega$, and $\gamma_o = \frac{Gm_e}{a^2}$ is the gravity acceleration on the Earth's surface. Furthermore, a is the Earth radius and θ and λ indicate colatitude and longitude, respectively.
The loads were restricted to those whose function can always be factorized in this way:

$$L(t,\theta,\lambda) = f(t)\sigma(\theta,\lambda), \tag{1.2}$$

where $f(t)$ is the load time-history and $\sigma(\theta,\lambda)$ is the load function, which defines the spatial extension of the load. According to the general CSH expansion theorem, for a generic NAX load it is always possible to write:

$$\sigma(\theta,\lambda) = \sum_{l=0}^{\infty}\sum_{m=-l}^{l}\sigma_{lm}Y_{lm}(\theta,\lambda), \tag{1.3}$$

where σ_{lm} are the CSH (Complex Spherical Harmonics) coefficients and are given by:

$$\sigma_{lm} = \int_{\Omega}\sigma(\theta,\lambda)Y^*_{lm}(\theta,\lambda)\,d\Omega, \tag{1.4}$$

and where $Y_{lm}(\theta,\lambda)$ are the spherical harmonics. From Equation (1.3) one can obtain the RSH (Real Spherical Harmonics) expansion, according to the RSH expansion theorem:

$$\sigma(\theta,\lambda) = \sum_{l=0}^{\infty}\sum_{m=0}^{+l}(c^{\sigma}_{lm}\cos(m\lambda) + s^{\sigma}_{lm}\sin(m\lambda))P_{lm}(\cos\theta), \tag{1.5}$$

where $P_{lm}(\cos\theta)$ are the Legendre orthogonal polynomials and where

$$\begin{pmatrix} c^{\sigma}_{lm} \\ s^{\sigma}_{lm} \end{pmatrix} = (2-\delta_{0m})\mu_{lm}\begin{pmatrix} & Re(\sigma_{lm}) \\ - & Im(\sigma_{lm}) \end{pmatrix} \text{ with } (l \geq 0, 0 \leq m \leq l), \tag{1.6}$$

with

$$\mu_{lm} = \sqrt{\frac{2l+1}{4\pi}\frac{(l-m)!}{(l+m)!}}. \tag{1.7}$$

1.2 The Viscoelastic Model

The Maxwell Rheology is the simplest viscoelastic model, but can reproduce the Earth behavior reasonably [Cathles, 1975]. In particular, a Maxwellian body is characterized by an elastic and a viscous component, respectively given by:

$$\epsilon_e = \frac{\sigma}{2G} \tag{1.8}$$

$$\dot{\epsilon}_v = \frac{\sigma}{2V}, \tag{1.9}$$

where σ is the applied stress, ϵ_e and $\dot{\epsilon_v}$ are the consequent elastic strain and viscous strain rate, while G and V are the shear modulus and the Maxwell viscosity, respectively.
The total strain rate is obtained by adding the time derivative of Equation (1.8) and Equation (1.9):

$$\dot{\epsilon} = \dot{\epsilon_e} + \dot{\epsilon_v} = \frac{\dot{\sigma}}{2G} + \frac{\sigma}{2V}. \tag{1.10}$$

Equation (1.10) can be solved by applying the Laplace transform to both sides of the equation:

$$s\left(\int_0^\infty e^{st}\epsilon(t)\,dt\right) - \epsilon(0) = \frac{s}{2G}\left(\int_0^\infty e^{st}\sigma(t)\,dt\right) - \sigma(0) + \frac{1}{2V}\left(\int_0^\infty e^{st}\sigma(t)\,dt\right). \tag{1.11}$$

By putting $\epsilon(0) = \sigma(0) = 0$ and $LT[\epsilon] = \int_0^\infty e^{st}\sigma(t)\,dt \equiv \epsilon(s)$, the following relation is obtained:

$$\epsilon(s) = \frac{\sigma(s)}{2G(s)} \text{ with } G(s) = \frac{Gs}{s + G/V}, \tag{1.12}$$

which is formally identical to the elastic relation shown in Equation (1.8).

1.3 Response to Surface Loads

The Laplace-transformed components of surface displacements can now be obtained by considering the general poloidal-toroidal decomposition of a solenoidal displacement field [Backus, 1986 and Sabadini et al., 1995]. In fact, the toroidal components were neglected because of the assumption of spherical symmetry, so that the Laplace-transformed components of the surface displacement induced by a NAX load acting upon a SVISG Earth can be written as:

$$\begin{pmatrix} u_r \\ u_\theta \\ u_\lambda \end{pmatrix}(s,a,\theta,\lambda) = \sum_{l=0}^{\infty}\sum_{m=-l}^{l} \begin{pmatrix} u_{lm} \\ v_{lm} \\ v_{lm} \end{pmatrix}(s,a) \cdot \begin{pmatrix} 1 \\ \partial_\theta \\ \frac{\partial_\lambda}{\sin\theta} \end{pmatrix} Y_{lm}(\theta,\lambda) \tag{1.13}$$

where u_{lm} and v_{lm} satisfy the constitutive equation:

$$\begin{pmatrix} u_{lm} \\ v_{lm} \end{pmatrix}(s,a) = \begin{pmatrix} c_l \\ d_l \end{pmatrix}(s)\sigma_{lm} f(s) \tag{1.14}$$

and where $f(s) = LT[f(t)]$, c_l, d_l are model-related constants, a is the Earth radius and σ_{lm} are the CSH coefficient of the load function, and are given by Equation (1.4).
In order to obtain an expression for u_{lm} and v_{lm} that is a function of known quantities, three results from literature need to be used [Spada, 2003b]:

1. The constitutive equation that describes the strain in response to a unit load ($L(t,\Theta) = \delta(t)\sigma^{\delta}(\Theta)$):

$$\begin{pmatrix} u_l \\ v_l \end{pmatrix}^{\delta}(s,a) = \begin{pmatrix} c_l \\ d_l \end{pmatrix}(s)\,\sigma_l^{\delta}; \tag{1.15}$$

2. the definition of load-deformation coefficients h_l and l_l:

$$\frac{1}{a}\begin{pmatrix} u_l \\ v_l \end{pmatrix}^{\delta}(s,a) \equiv \frac{m_s^{\delta}}{m_e}\begin{pmatrix} h_l \\ l_l \end{pmatrix}(s),\ l \geq 2 \tag{1.16}$$

   where m_s^{δ} is the static mass of the unit load and m_e is the mass of the Earth;

3. the coefficients of the expansion on Legendre polynomials of the unit load function:

$$\sigma_l^{\delta} = m_s^{\delta}(\frac{2l+1}{4\pi a^2}). \tag{1.17}$$

In fact, by inverting Equation (1.15), one obtains an expression for c_l, d_l as a function of unit-load reletad quantities, which can be replaced with the expressions given by Equations (1.16) and (1.17), so that one obtains:

$$\begin{pmatrix} c_l \\ d_l \end{pmatrix}(s) = \frac{1}{\sigma_l^{\delta}}\begin{pmatrix} u_l \\ v_l \end{pmatrix}^{\delta}(s,a) = \frac{4\pi a^3}{m_e(2l+1)}\begin{pmatrix} h_l \\ l_l \end{pmatrix}(s) \tag{1.18}$$

when inserted into Equation (1.14), this formula gives an expression for u_{lm} and v_{lm} that has to be inserted into Equation (1.13). Now, by considering the facts that $\rho_e = 3m_e/(4\pi a^2)$ is the average density of the Earth, and that

$$\begin{pmatrix} h_l \\ l_l \end{pmatrix}(s) f(s) = \begin{pmatrix} h_l \\ l_l \end{pmatrix}(t) \otimes f(t) \equiv \begin{pmatrix} \bar{h}_l \\ \bar{l}_l \end{pmatrix}(t), \tag{1.19}$$

equation (1.13) becomes:

$$\begin{pmatrix} u_r \\ u_\theta \\ u_\lambda \end{pmatrix}(t,a,\theta,\lambda) = \frac{3}{\rho_e}\sum_{l=0}^{\infty}\sum_{m=-l}^{l}\frac{\sigma_{lm}}{2l+1}\begin{pmatrix} \bar{h}_l \\ \bar{l}_l \\ \bar{l}_l \end{pmatrix}(t)\begin{pmatrix} 1 \\ \partial_\theta \\ \frac{\partial_\lambda}{\sin\theta} \end{pmatrix} Y_{lm}(\theta,\lambda). \tag{1.20}$$

By applying Equations (1.5) and (1.6), one can obtain the Laplace-Transformed expression for Equation (1.20) with real coefficients, so that Equation (1.20) becomes:

$$\begin{aligned}\begin{pmatrix} u_r \\ u_\theta \\ u_\lambda \end{pmatrix}(t,a,\theta,\lambda) \equiv \frac{3}{\rho_e}\sum_{l=0}^{\infty}\sum_{m=0}^{+l}\frac{1}{(2l+1)}\begin{pmatrix} \bar{h}_l \\ \bar{l}_l \\ \bar{l}_l \end{pmatrix}(t)\begin{pmatrix} c^\sigma_{lm}\cos(m\lambda)+s^\sigma_{lm}\sin(m\lambda) \\ c^\sigma_{lm}\cos(m\lambda)+s^\sigma_{lm}\sin(m\lambda) \\ s^\sigma_{lm}\cos(m\lambda)-c^\sigma_{lm}\sin(m\lambda) \end{pmatrix} \\ \cdot\begin{pmatrix} 1 \\ \partial_\theta \\ \frac{\partial_\lambda}{\sin\theta} \end{pmatrix} P_{lm}(\cos\theta),\end{aligned} \tag{1.21}$$

where c^σ_{lm} and s^σ_{lm} are given by Equation (1.6). In this investigation, only AX loads were taken into account.

1.4 Response to AX Loads

In order to derive the Earth response to AX loads, it is useful to take into consideration the symmetry of the problem. In particular, the load function $\sigma(\theta,\lambda)$ can be defined in another frame called "load reference frame" (LRF), in which the symmetry axis of the load coincides with the z-axis and where the pole of the load is defined as the intersection between the load and the z-axis. In this frame, the load function depends on a new colatitude only, Θ, which is defined as follows:

$$\cos\Theta_p = \cos\theta_p\,\cos\theta_c + \sin\theta_p\,\sin\theta_c\cos(\lambda_p-\lambda_c), \tag{1.22}$$

where (θ_p,λ_p) and (θ_c,λ_c) are the spherical coordinates of the point P and of the pole of the load, as measured in the Geographical Reference Frame (GRF).
In the LRF, the expansion of the load function in Legendre polynomials can be written as:

$$\sigma^{AX}(\Theta) = \sum_{l=0}^{\infty}\sigma_l^{AX}P_l(\cos\Theta), \tag{1.23}$$

where

$$\sigma_l^{AX} = \frac{2l+1}{2}\int_0^\pi \sigma^{AX}(\Theta)P_l(\cos\Theta)\sin\Theta d\Theta. \tag{1.24}$$

Using the addition theorem, it is possible to link the coefficients of the LEG expansion σ_l^{AX} in LRF to the CSH coefficients σ_{lm}^{ax} in GRF. In particular, Equation (1.23) becomes:

$$\sigma^{AX}(\Theta) \equiv \sigma^{ax}(\theta,\lambda) = \sum_{l=0}^{\infty}\sum_{m=-l}^{l} \sigma_{lm}^{ax} Y_{lm}(\theta,\lambda), \tag{1.25}$$

with

$$\sigma_{lm}^{ax} = \frac{4\pi Y_{lm}^*(\theta_c,\lambda_c)}{2l+1}\sigma_l^{AX}. \tag{1.26}$$

This expression can be put into Equation (1.6) so as to determine the analytic expression for c_{lm}^{σ} and s_{lm}^{σ} which, inserted into Equation (1.21) gives:

$$\begin{aligned}\begin{pmatrix} u_r \\ u_\theta \\ u_\lambda \end{pmatrix}^{ax}(t,a,\theta,\lambda) =& \frac{3}{\rho_e}\sum_{l=0}^{\infty}\sum_{m=0}^{+l}\begin{pmatrix} \bar{h}_l \\ \bar{l}_l \\ \bar{l}_l \end{pmatrix}(t)\frac{2-\delta_{0m}}{2l+1}\frac{(l-m)!}{(l+m)!}\sigma_l^{AX}P_{lm}\cos\theta_c \\ & \begin{pmatrix} \cos m(\lambda-\lambda_c) \\ \cos m(\lambda-\lambda_c) \\ -\sin m(\lambda-\lambda_c) \end{pmatrix}\begin{pmatrix} 1 \\ \partial_\theta \\ \frac{m}{\sin\theta} \end{pmatrix} P_{lm}(\cos\theta).\end{aligned} \tag{1.27}$$

The LEG expansion (Equation (1.23)) is particularly useful to calculate the static mass m_s of the load, which is given by:

$$m_s \overset{def}{=} \int_\Omega \sigma(\theta,\lambda)\,dA \overset{Eq.1.23}{=} 2\pi a^2\int_0^\pi \sigma^{AX}(\Theta)\sin\Theta d\Theta = 4\pi a^2\sigma_0^{AX}. \tag{1.28}$$

From the static mass it is possible to determine the dynamic mass of the load:

$$\mu(t) \overset{def}{=} \int_\Omega L(t,\theta,\lambda)\,dA = f(t)m_s. \tag{1.29}$$

Note that the first definitions of Equations (1.28) and (1.29) are true for NAX loads as well.
The principle of mass conservation is ensured by introducing a complementary load such that the total dynamic mass of the system is identically null. In particular, it has to be:

$$\mu_T(t) = \mu^1(t) + \mu^2(t) = f^1(t)m_s^1 + f^2(t)m_s^2 \equiv 0 \tag{1.30}$$

where $\mu^1(t)$ is the dynamic mass of the "primary" load and $\mu^2(t)$ is the dynamic mass of the "secondary" load. Equation (1.30) can be satisfied by the condition:

$$\begin{cases} f^1(t) = f^2(t) \\ m_s^1 = -m_s^2. \end{cases} \tag{1.31}$$

In other words, the primary and secondary load need to have the same time history but opposite static masses. Conventionally, $m_s^1 \geq 0$ and is associated with an excess of mass on the Earth, such as an ice sheet. Thus, $m_s^2 \leq 0$ and is related to a mass deficiency, such as sea level drop due to ice formation. In the TABOO program, the secondary load is realized by introducing a complementary disk load with negative height on the ocean surface.
In this investigation, only two load geometries were used, and they both have axial symmetry: the disk and the parabola. A graphical representation of these two scenarios was shown in Figure 1.1.

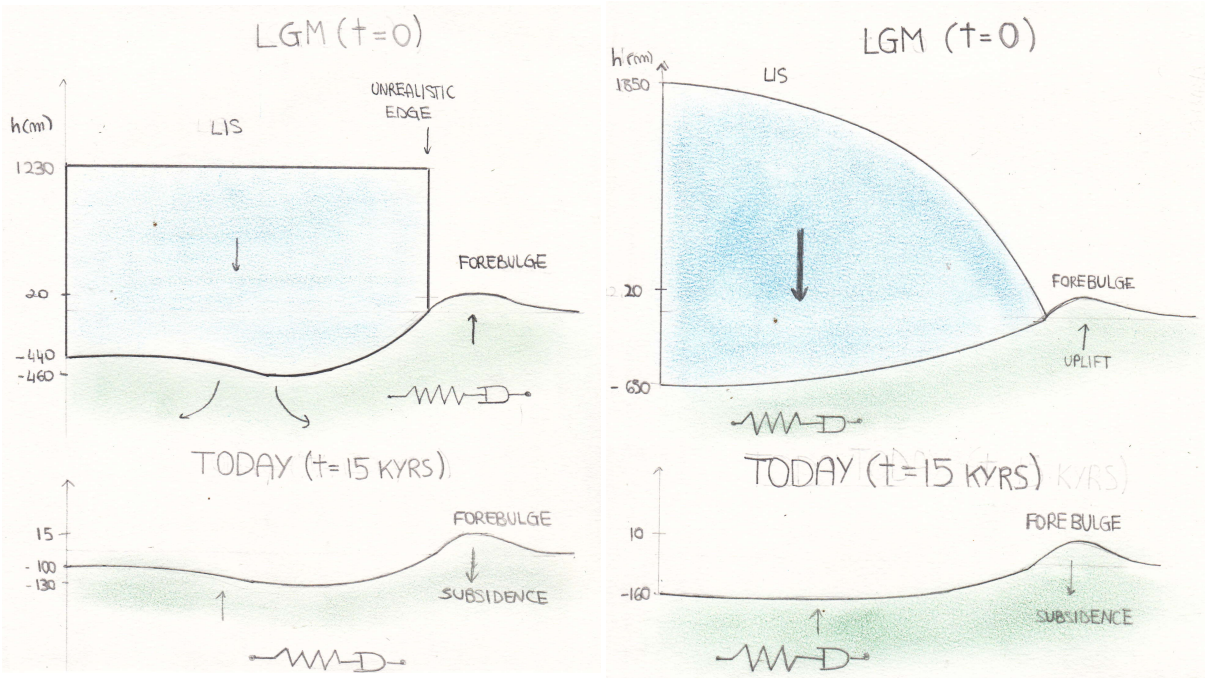

(a) (b)

Figure 1.1: Forebulge induced by a disk load (Figure 1.1a) and by a parabolic load (Figure 1.1b) at Last Glacial Maximum (t = 15 kyrs) and at present time (t = 0).

The Balanced Disk Load

The load function for a disk load in the LRF is given by:

$$\sigma^d(\Theta) = \begin{cases} \rho_i h & 0 \leq \Theta \leq \alpha \\ 0 & \alpha < \Theta \leq \pi, \end{cases} \tag{1.32}$$

where ρ_i is the density of the load, h is its maximum height and α is its angular half-amplitude.

By replacing this expression into the third equivalence of Equation (1.28), it is immediate to obtain the static mass of the disk, which is given by:

$$m_s^d = 2\pi a^2 \rho_i h(1 - \cos\alpha). \tag{1.33}$$

The disk load is balanced by a secondary disk load which satisfies Equation (1.31); by imposing this condition, one obtains the following load function:

$$\sigma^c(\Theta) = \begin{cases} 0 & 0 \leq \Theta \leq \alpha \\ \rho_i h' & \alpha \leq \Theta \leq \pi, \end{cases} \tag{1.34}$$

where

$$h' = h\Big(\frac{\cos\alpha - 1}{\cos\alpha + 1}\Big). \tag{1.35}$$

The load function for the balanced disk load is then obtained by adding Equations (1.32) and (1.34):

$$\sigma^{cd}(\Theta) = \rho_i h \begin{cases} 1 & 0 \leq \Theta \leq \alpha \\ \frac{\cos\alpha - 1}{\cos\alpha + 1} & \alpha \leq \Theta \leq \pi, \end{cases} \tag{1.36}$$

which, inserted into Equation (1.24), gives the LEG expansion coefficients for a balanced disk load:

$$\sigma_l^{cd} = \begin{cases} 0 & l = 0 \\ \frac{P_{l-1}(\cos\alpha) - P_{l+1}(\cos\alpha))}{1+\cos\alpha} & l \geq 1. \end{cases} \tag{1.37}$$

Then, this result must be inserted into Equation (1.27) to obtain the Earth response to a balanced disk load.

The Balanced Parabolic Load

The idea behind the analytic expression for the balanced parabolic load is the same as the one for the balanced disk load; therefore, only the main results were written [Yuen et al., 1986]. In particular, the load function for the balanced parabolic load is given by:

$$\sigma^{cp} = \rho_i \begin{cases} h_o\sqrt{\frac{\cos\Theta - \cos\alpha}{1-\cos\alpha}} & 0 \leq \Theta \leq \alpha \\ h' & \alpha < \Theta \leq \pi, \end{cases} \tag{1.38}$$

where

$$h' = -\frac{2}{3}\left(\frac{1 - \cos\alpha}{1 + \cos\alpha}\right)h_0, \tag{1.39}$$

with α being the angular half-amplitude of the parabolic load, and h_0 being the load thickness at $\Theta = 0$.
The corresponding LEG coefficients are given by:

$$\sigma_l^{cp} = \rho_i h \begin{cases} 0 & l = 0 \\ \frac{\rho_i h_0}{3}(1-\cos\alpha)\xi_l(\alpha) + \frac{\rho_i h'}{2}[P_{l+1}(\cos\alpha) - P_{l-1}(\cos\alpha)] & l \geq 1, \end{cases} \tag{1.40}$$

where

$$\xi_l(\alpha) = -\frac{3}{4(1-\cos\alpha)^2}\left[\frac{T_{l+1}(\alpha) - T_{l+2}(\alpha)}{l+3/2} - \frac{T_{l-1}(\alpha) - T_l(\alpha)}{l-1/2}\right], \tag{1.41}$$

where $T_l(\alpha)$ are the Chebichev polynomials of second kind.
Finally, the static mass of the primary load is given by

$$m_s^p = \frac{4}{3}\pi a^2 \rho_i h_0 (1-\cos\alpha). \tag{1.42}$$

2. Method

2.1 Model

The dynamic of the forebulge was studied through its radial displacements as well as their corresponding rates. The evolution of these physical quantities was determined by numerical simulations performed by the TABOO program, which allows the user to set the Earth's model, the load geometry, its time history and the type of study. To define the outline of the evolution, the following choice of parameters was made:

1. **Earth model**:
   The lithosphere is 70 km thick and the mantle is made of three viscosity layers. Therefore, the upper shallow mantle is divided into two layers of viscosity $1.0 \cdot 10^{21} Pa \cdot s$, while the lower mantle is made of one layer of viscosity $2.0 \cdot 10^{21} Pa \cdot s$ [Mitrovica, 1996]. The Earth's density and rigidity profile used was employed by the GIA Benchmark group [Spada et al., 2011], and it was explained in more detail in Table 2.1.

	Radius (km)	Density (kg/m^3)	Shear Modulus ($Pa \cdot 10^{11}$)
LT	6371	3037	0.50605
ML1	6301	3438	0.70363
ML2	5951	3871	1.0549
ML3	5701	4978	2.2834
CORE	3480	10750	0.0

Table 2.1: Density and rigidity profile of a horizontally homogeneous Earth assuming that the lithosphere is 70 km thick. Label LT stands for "Lithosphere" while MLn, n =1, 2, 3 stands for Mantle Layer number n. In the column labelled by "Radius", the distance (km) between the centre of the Earth and the top of the corresponding layer is displayed. In the second and third columns the density (kg/m^3) and shear modulus ($Pa \cdot 10^{11}$) of the corresponding layers are displayed, respectively.

2. **Load geometry:**
   The glacial load has a quasi-parabolic shape and an angular amplitude of 10° in lateral direction, and it is placed at the North Pole. Furthermore, a complementary disk load (i. e. a load of uniform thickness) is added in the region outside the load so as to ensure the conservation of mass.

3. **Load Time history:**
   The following function describes the load's time history, which was referred to as "simple deglaciation":

$$f(t) = \begin{cases} h & \text{if } t < 0 \\ h\left(1 - \frac{t}{\tau}\right) & \text{if } 0 \leq t < \tau \\ 0 & \text{if } t \geq \tau, \end{cases} \tag{2.1}$$

   where h is the ice thickness at t $\leq$ 0, which was set at 2500 m [Spada and Melini, 2025], while τ defines the length of the deglaciation and was set at 10 kyrs [Motoyama et al., 2007]. This time history establishes the condition of isostatic equilibrium at the Last Glacial Maximum (LGM), which is perturbed during the uniform deglaciation that occurs at the constant rate of $1/\tau$. This function was represented in Figure 2.1.

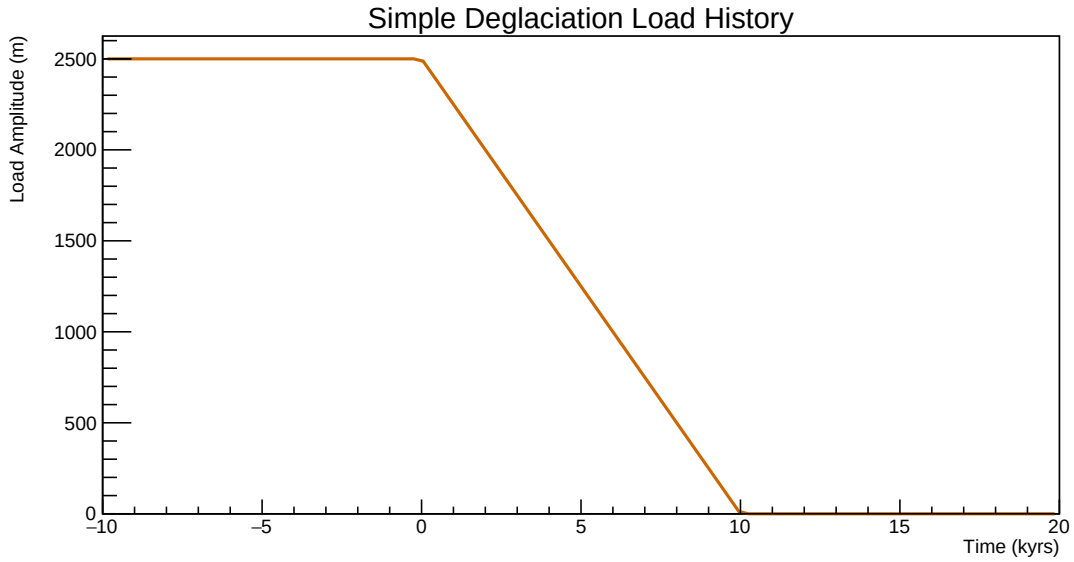

Figure 2.1: Graphical representation of the simple deglaciation function. The load is still unitl t = 0, when it starts melting at a constant rate given by 0.1 $kyrs^{-1}$, until at t = 10 kyrs it disappears.

4. **Study:**
   The type of investigation is a local study which consists of computing the analysis on points regularly separated by 0.1° along a fixed meridian (0 meridian) and included between 0° and 30° along colatitude. The analysis is computed at t = 15 kyrs, which corresponds to present time according to the time convention used for this investigation [Severinghaus and Brook, 1999].

Later on, this choice of parameters was referred to as "model 0". Even though for this investigation only radial displacements and rates were used, in Figure 2.2 all the quantities that TABOO can compute (radial, colatitudinal, longitudinal displacements and geoid's height displacement) were shown. In Figure 2.3, the rates of the above-mentioned quantities were shown. All these quantities were plotted as functions of colatitude, and this format was kept for all TABOO simulations performed for this investigation.

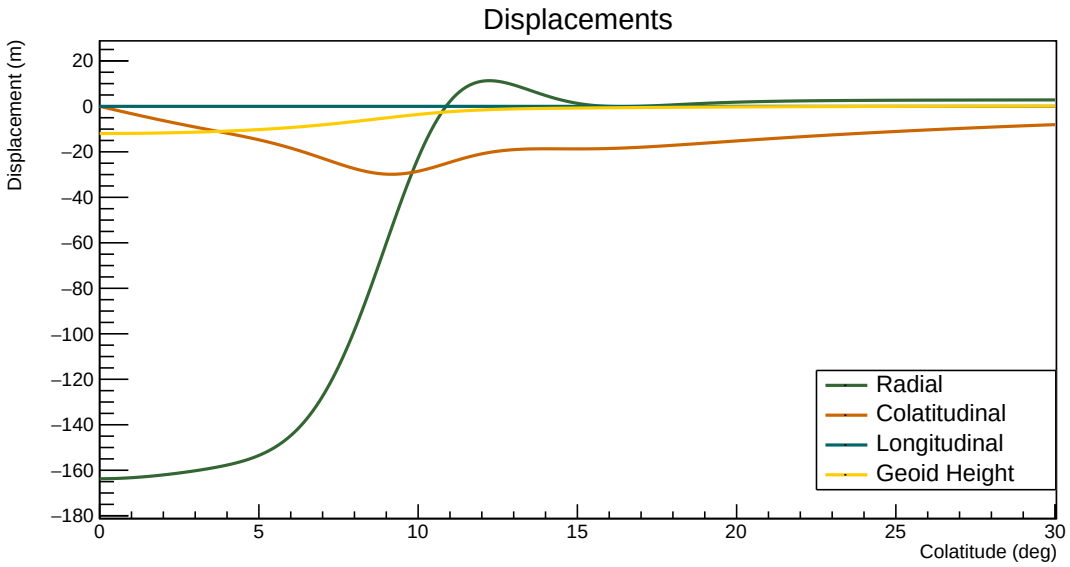

Figure 2.2: Radial (green), colatitudinal (red), longitudinal (blue) displacements and geoid height (yellow) as functions of colatitude computed by setting the parameters of model 0 (with t = 15 kyrs, which corresponds to present time according to the time convention used for this investigation).

Furthermore, the implications of the assumption of spherical symmetry, on which TABOO simulations are based, were specified [Spada, 2003b]:

1. The load position does not affect the computed analysis. Therefore, for the sake of simplicity it was placed at the North Pole of the Earth model;

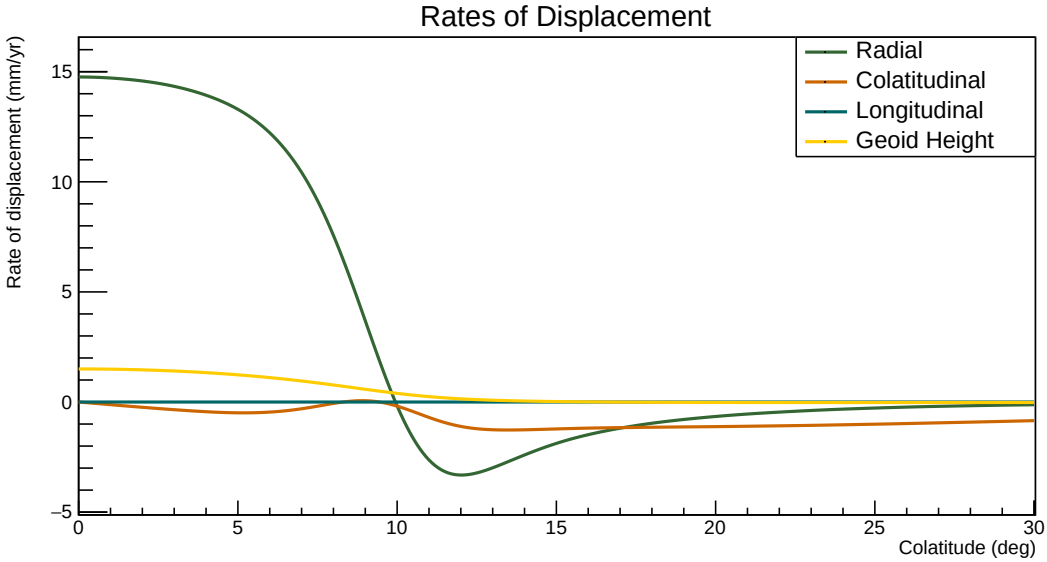

Figure 2.3: Radial (green), colatiudinal (red), longitudinal (blue) rates of displacement and rate of geoid height variation (yellow) as functions of colatitude computed by setting the parameters of model 0 (with t = 15 kyrs, which corresponds to present time according to the time convention used for this investigation).

2. the longitudinal displacement and its rate are always zero, as shown in Figure 2.2 and Figure 2.3;

3. the meridian along which the analysis is computed does not affect the obtained results, as the load is axis-symmetric [Farrel, 1972].

To add to this, starting from the ice thickness set in Load History and the load shape and angular half-amplitude set in Load Geometry, TABOO provides an estimate of the maximum load mass by using Equation (1.42) where $\rho_i = 931\ kg/m^3$ is the ice density. The resulting mass was found to be around $6.01 \cdot 10^{18}$ kg, a compatible value with the estimated maximum mass of the Laurentide Ice Sheet (LIS), which is of the order of 10^{19} kg [Moreno-Parada et al., 2023].

2.2 Forebulge Time Evolution

To investigate the dynamics of the forebulge, the only parameter of the Earth and ice cap models that needed to be changed was the instant t at which the analysis is computed. To plot an outline of the temporal evolution, t was varied between 0 kyrs and 25 kyrs through increments of 1 kyr each. By comparing the graphs plotted for each t, it was possible

to obtain an outline of the temporal evolution of lithosphere deformations induced by glacial unloading. To have a clearer view of the evolution of the forebulge, the graphs were zoomed in on the lateral upheaval by setting the following ranges:

1. $[9, 30]^\circ$ colatitude on the x-axis for both the radial displacements and their rates;
2. $[-15, 35]$ m for the radial displacements;
3. $[-5, 5]$ mm/yr for the rates of the radial displacements.

The evolution of the forebulge was quantified by tracking the movements of its peak. To do this, the following quantities were recorded:

1. The instant at which the analysis is computed;
2. the colatitude at which the maximum amplitude is found;
3. the maximum amplitude;
4. the corresponding rate of radial displacement.

Through such data, it was possible to quantify both vertical and horizontal displacement of the peak over time.

2.3 Current Land Subsidence and Rising Sea Level

The impact of the forebulge collapse on rising sea level was studied through its evolution from today (t = 15 kyrs) to the next two centuries (t = 15.2 kyrs), by increments of 50 years each. Thus, TABOO simulations were performed to obtain the radial displacements and their rates for each instant t. Initially, the two types of graphs were analyzed by recording the minimum rate of radial displacement, its colatitude and the corresponding radial displacement found in the uplifted region next to the load.
After that, a more general analysis was conducted by finding the radial displacement rates every 0.1° colatitude in the forebulge region. These data were used to create two charts. The first one has the following characteristics:

1. The radial displacements as a function of colatitude, computed at t = 15 kyrs, are displayed, so as to have a visual representation of the forebulge;
2. every 0.1° colatitude (the interval at which the analysis is computed, set in the local study) a down arrow is drawn with color shades from yellow to red. To each shade of color corresponds one of the following ranges:

(a) [0, 1] mm/yr;

(b) [1, 2] mm/yr;

(c) [2, 3] mm/yr;

(d) [3, 3.5] mm/yr;

where the absolute values of the subsidence rates were used.

3. the range of the x axis is $[9, 16.5]^\circ$ colatitude, in order to display the whole subsidence region.

The second chart is very similar to the first one, but:

1. The range of the x axis is $[10, 16.5]^\circ$, so as to display the forebulge region, where the radial displacements are positive for definition since the forebulge identifies the upheaval;

2. In addition to the radial displacements computed at t = 15 kyrs, there is a curve representing the same quantity calculated at t = 15.2 kyrs, in order to visualize the entity of land subsidence in the forebulge region.

Note that in fact, according to TABOO's simulations, the subsidence regions covers the interval $[9, 30]^\circ$; however, for a matter of visibility, the rates were computed only until 16.5°, so as to focus on the forebulge region.
Then, the maximum rate of subsidence computed for t = 15 kyrs was assumed constant and compared with experimental data from the Permanent Service for Mean Sea Level [Holgate et al., 2013], which distributes annual and monthly tide gauge records from various stations throughout the world. In particular, the comparison was made with records from New York The Battery station [PSMSL, 2025c], which is located close to the top of the LIS-related forebulge [Brandes et al., 2025] and shows a high subsidence rate, equal to (2.90 ± 0.12) mm/yr [PSMSL, 2025a]. This value was obtained using monthly data from 1856 to 2024 referred to the Revised Local Reference (RLR, 6.98 m below the Mean Sea Level calculated between 1964 and 2005 for New York The Battery), a common datum to which each mean value is reduced to in order to calculate time series [PSMSL, 2025b]. However, a discrepancy of (1.3 ± 0.7) mm/yr is expected between TABOO predictions and experimental data, as this is the average contribution of climate change and current ice melting to rising sea level [Gornitz et al., 2001]. Note that TABOO data represent the vertical land movement; therefore, the subsidence rate was changed in sign so that the value could be connected with the annual trend of RSL.

2.4 Controlling Parameters of the Forebulge

The glacial forebulge was studied further by varying the parameters of model 0, in order to determine its controlling factors and the role of each parameter in determining the forebulge shape and its subsidence rates.

Load history

The load history chosen for model 0 is extremely simplistic, since it assumes the condition of equilibrium at LGM and neglects the duration of the load formation. However, there is proof that this assumption leads to unrealistic results, which are referred to as the strain rate-stress paradox[Brandes et al., 2025]. For this reason, the radial displacements and the corresponding rates were analysed by considering a more realistic time history, which is referred to as "saw tooth" and which is given by:

$$f(t) = \sum_{n=0}^{N} f_n(t), \tag{2.2}$$

where $N \geq 0$ is the number of glaciation in addition to the last and where

$$f_n(t) = [\mathcal{H}(t + n\theta + \tau) - \mathcal{H}(t + n\theta)] f_n^{\uparrow}(t) + [\mathcal{H}(t + n\theta) - \mathcal{H}(t + n\theta - \delta)] f_n^{\downarrow}(t), \tag{2.3}$$

with $-\tau \leq t \leq -n\theta + \delta$.
In Equation (2.3), $\mathcal{H}(t)$ denotes the step function, τ is the length of each loading phase and δ is the length of the unloading phase; $\theta \equiv \tau + \delta$ and:

$$f_n^{\uparrow}(t) = +\frac{t}{\tau} + \frac{n\theta + \tau}{\tau} \tag{2.4}$$

$$f_n^{\downarrow}(t) = -\frac{t}{\delta} - \frac{n\theta - \delta}{\delta}. \tag{2.5}$$

In particular, two investigations were performed:

1. The first one was meant to study the impact of different loading times. Therefore, the closest case to model 0 was chosen, with n = 1, δ = 10 kyrs and h = 2500 m. Three different loading times were chosen: $\tau_1 = 10$ kyrs, $\tau_2 = 30$ kyrs and $\tau_3 = 90$ kyrs. This choice of parameters, which differs from model 0 only for the presence of 1 glaciation in addition to the last, is referred to as "model 1";

2. the second one was meant to investigate the radial displacements and their rates obtained by making a suitable choice of parameters for the Laurentide Ice Sheet. Therefore, the loading time τ was set at 90 kyrs, while the number of glaciations in addition to the last was set at 8, for a total number of glaciations equal to 9 [Motoyama et al., 2007]. This choice of parameters was referred to as "model 2".

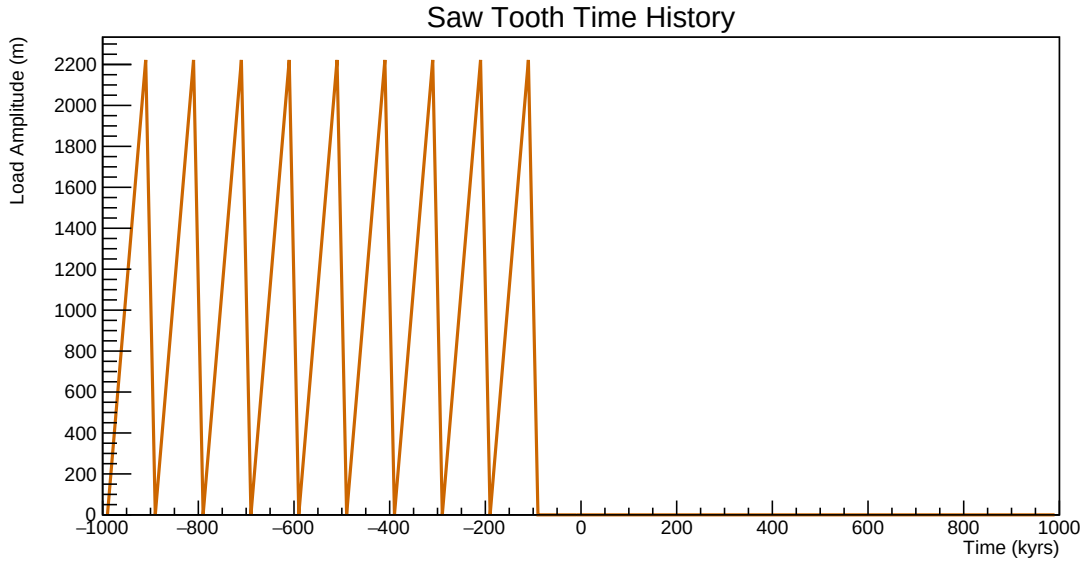

Figure 2.4: Graphical representation of the Saw Tooth time history. This funtion was obtained by choosing n = 8, $\tau = 90$ kyrs and $\delta = 10$ kyrs.

Load Geometry

Load with different shapes and amplitudes were used to compute the corresponding radial displacements and rates. In particular, model 0 was compared with:

1. Model 3: a disk load with the same mass and amplitude. In order to obtain the maximum height that realizes such a configuration, Equation (1.33) (with $\rho_i = 931\ kg/m^3$), which gives the static mass for a disk load, was inverted. In particular, the maximum height h was found to be 1667 m;

2. model 4: a parabolic load with the same maximum thickness but half as wide. In particular, in this case the two ice caps do not have the same mass because, being the second one only 5° wide, this choice would have led to an unrealistically tall ice sheet.

In both models 3 ad 4, a complementary load is added to ensure the mass conservation.

Earth Model

Finally, the lithosphere thickness and the viscosity of the mantle layers were varied in order to analyze the dependence of the forebulge on these parameters.
Since the density and shear moduli profile used so far (see Table 2.1) does not allow to set the lithospheric thickness, the following computation was performed by using the

density and rigidity profile shown in Table 2.2, which was built ad hoc for TABOO [Spada, 2003a]. In particular, the lithosphere thickness was set at the following values

	Radius (km)	Density (kg/m^3)	Shear Modulus ($Pa \cdot 10^{11}$)
LT	6371	P-A	P-A
ML1	6371 - h	P-A	P-A
ML2	5971	3857.7	0.735
ML3	5701	4877.9	1.064
CORE	3480	10931.7	0.0

Table 2.2: Density and rigidity profile of a horizontally homogeneous Earth, where the lithospheric thickness h can be set by the user. The label LT stands for "Lithosphere" while MLn, n = 1, 2, 3 stands for Mantle Layer number n. In the column labeled by "Radius", the distance (km) between the centre of the Earth and the top of the corresponding layer is displayed. In the second and third column the density (kg/m^3) and shear modulus ($Pa \cdot 10^{11}$) of the corresponding layers are displayed. This model is fully Prem-Averaged (P-A), except fore the core shear modulus, which was purposely set to 0 [Spada, 2003a].

[Turcotte and Gerald, 2014]:

1. 70 km, which is the average lithosphere thickness of the Earth;
2. 40 km, which is a suitable value for the oceanic lithosphere;
3. 120 km, which is a suitable value for the continental lithosphere;

Both configurations 2. and 3. were referred to as "model 5", as they differ from model 0 only for the lithospheric thickness (and, consequently, for the density and rigidity profile). Configuration 1 was referred to as model 0 in spite of the different density and rigidity profile. In particular, case 3. is locally realistic when analysing the deformations induced on the North American plate, whose continental lithosphere is anomalously thick [Zhao, 2013].
Then, the role of the viscosity of the mantle layers was investigated. In order to perform this task, the number of viscosity layers was not varied. Furthermore, the radii of each layer, their density and shear moduli were maintained constant, as TABOO does not allow the user to change these parameters one at time. This task was performed in two ways:

1. All three viscosity layers were proportionally modified (model 6). In particular, the two following configurations were used:

(a) $\eta_1 = 0.1 \cdot 10^{21} Pa \cdot s, \eta_2 = 0.1 \cdot 10^{21} Pa \cdot s, \eta_3 = 0.2 \cdot 10^{21} Pa \cdot s$;

(b) $\eta_1 = 10 \cdot 10^{21} Pa \cdot s, \eta_2 = 10 \cdot 10^{21} Pa \cdot s, \eta_3 = 20 \cdot 10^{21} Pa \cdot s$;

2. only the first viscosity layer was modified (model 7). In particular, the two following configurations were used:

   (a) $\eta_1 = 0.1 \cdot 10^{21} Pa \cdot s$;

   (b) $\eta_1 = 10 \cdot 10^{21} Pa \cdot s$.

Again, the point b) of option 2 is particularly suitable for the North American plate, whose continental lithosphere is anomalously thick [Zhao, 2013].

3. Results

3.1 Forebulge Time Evolution

In Figures 3.1a and 3.1b, the temporal evolutions from 0 to 25 kyrs of the radial displacement and its rate were shown. These graphs are meant to help visualise the entity of the process as a whole, since it is responsible for both a tough where the load would be and the forebulge.
From Figures 3.2a and 3.2b, it was possible to qualitatively describe the temporal evolution of the forebulge:

1. **0 kyrs $\leq$ t $<$ 8 kyrs:**
   During the deglaciation of the load, the forebulge continues to rise while slowly moving inwards. In this phase, the rate of rising continuously decreases.

2. **8 kyrs $\leq$ t $\leq$ 10 kyrs:**
   After reaching its maximum amplitude, the forebulge starts collapsing while it keeps moving inwards.

3. **10 kyrs $<$ t $\leq$ 15 kyrs:**
   The load has disappeared, while the forebulge continues collapsing and moving inwards. This is what has been happening since the disappearance of the Laurentide Ice Sheet until today. At t = 13 kyrs, the rate of lowering reached its maximum. Since then, the rate of subsidence continuously decreases in absolute value.

4. **15 kyrs $<$ t $\leq$ 25 kyrs:**
   The forebulge continues to collapse and reverses its horizontal migration, moving outwards. The collapse is irreversible and continues even when the upheaval goes below 0 m. This is what is going to happen in the next ten thousands of years.

The graphs in Figures 3.3 were made in order to better visualize the temporal evolution of the radial displacements and the corresponding rates for each temporal interval defined by points 1 - 4 above.

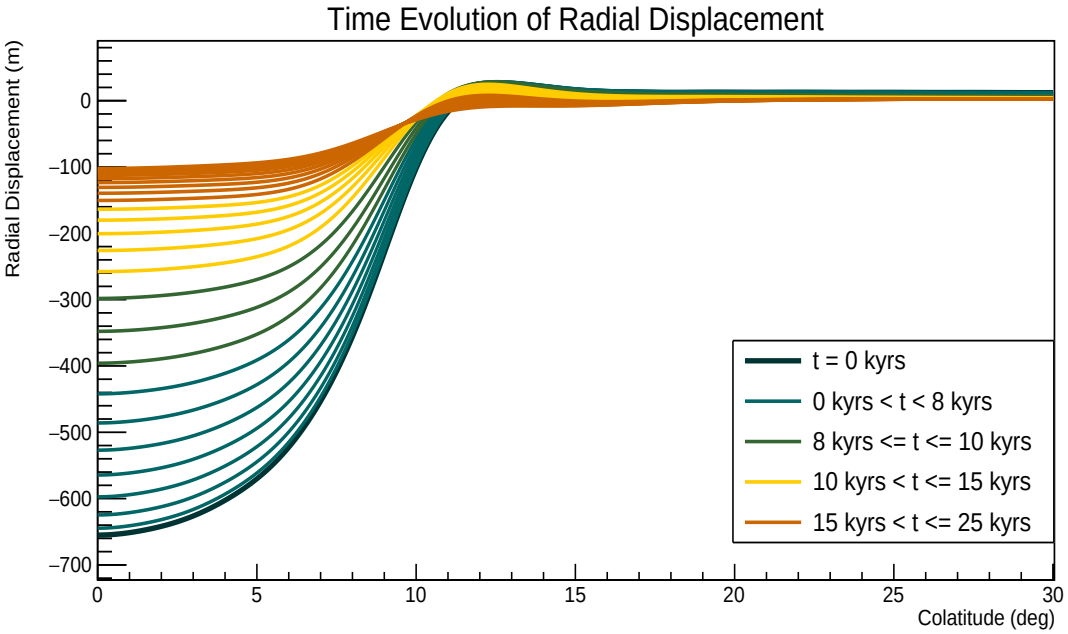

(a)

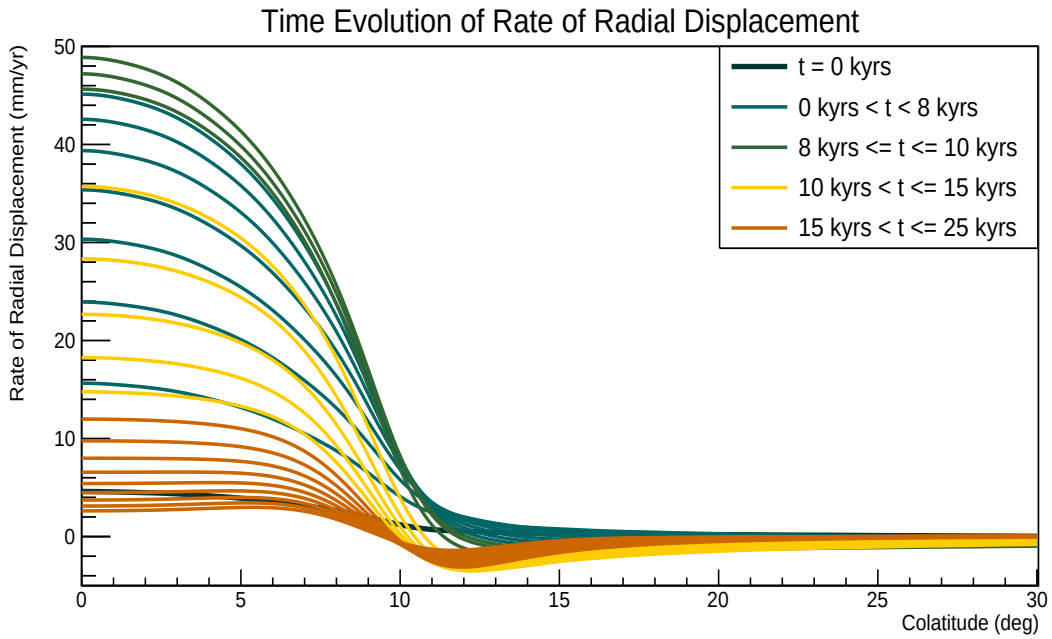

(b)

Figure 3.1: Temporal evolution of radial displacement (Figure 3.1a) and the corresponding rates (Figure 3.1b) from 0 to 25 kyrs. The dark, thick line corresponds to t = 0 kyrs, which is the starting point of the evolution.

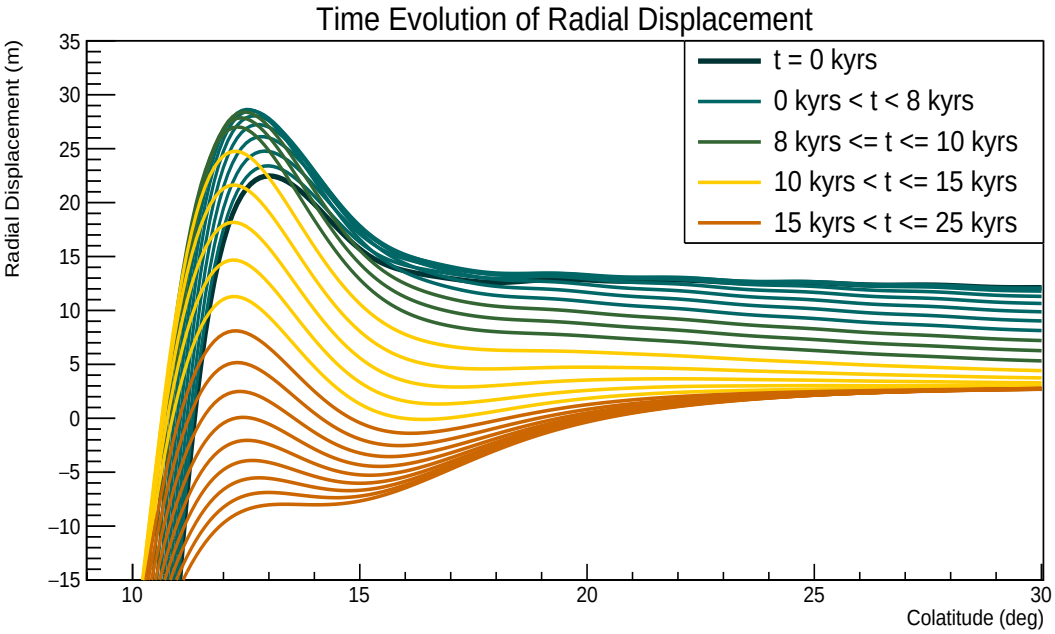

(a)

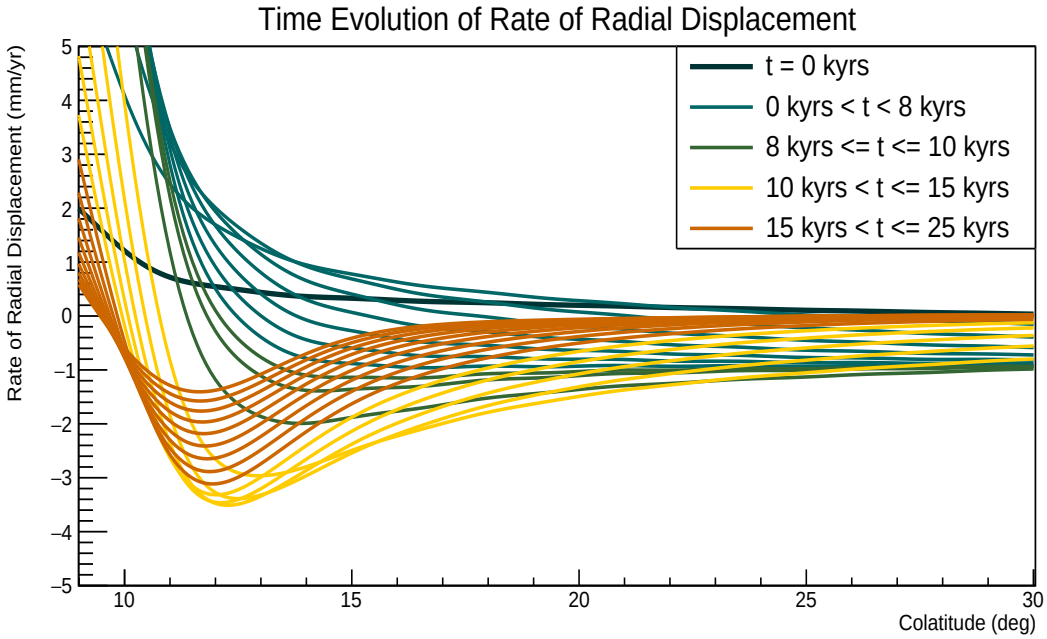

(b)

Figure 3.2: Temporal evolution of radial displacement (Figure 3.2a) and the corresponding rates (Figure 3.2b) of the forebulge from 0 to 25 kyrs. The dark, thick line corresponds to t = 0 kyrs, which is the starting point of the evolution.

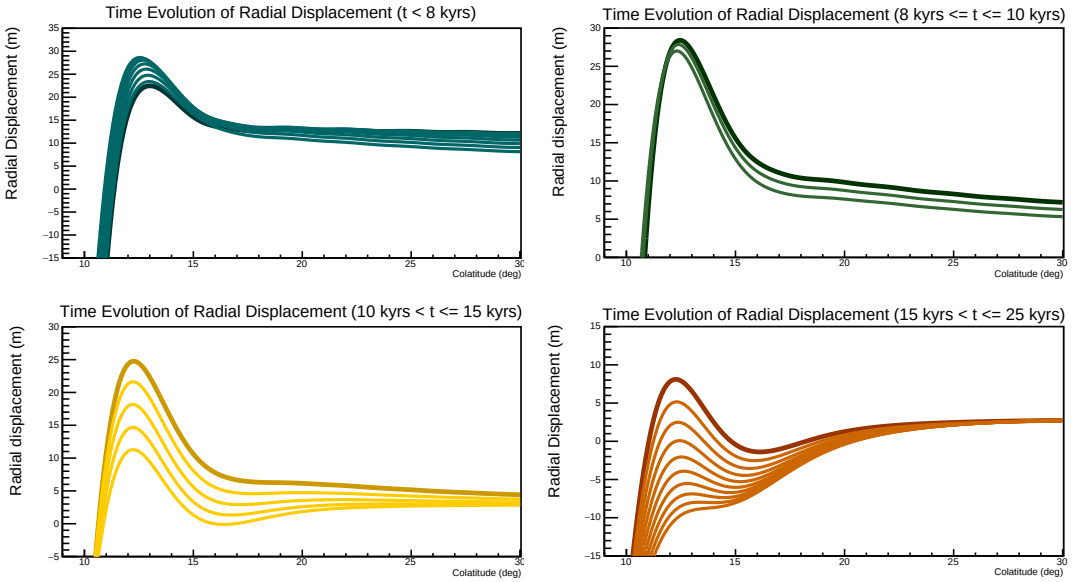

(a)

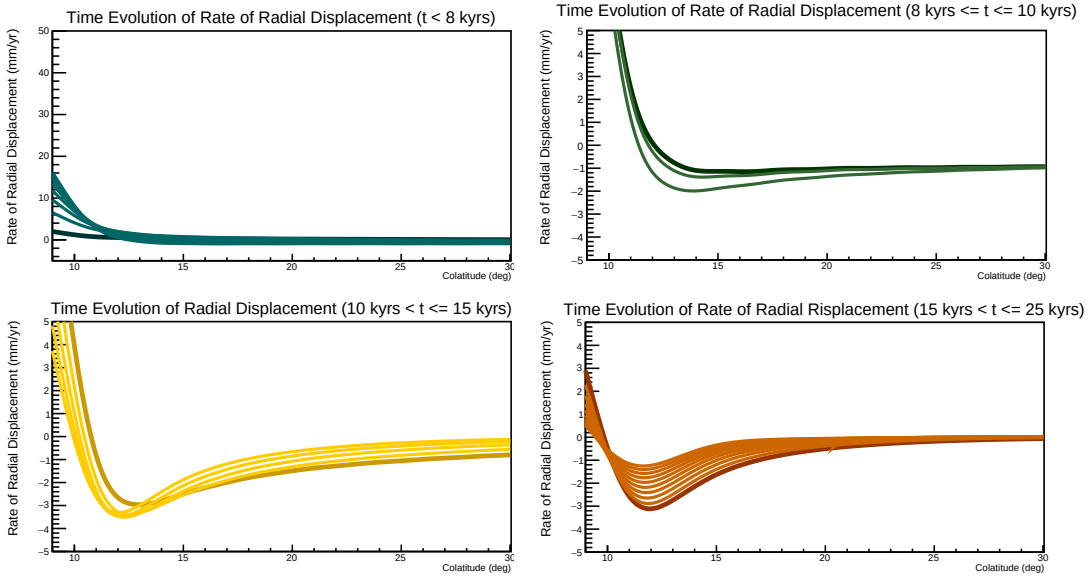

(b)

Figure 3.3: Temporal evolution of radial displacements (Figure 3.3a) and their rates (Figure 3.3b) divided in four categories: $t < 8$ kyrs (blue), 8 kyrs $\leq t \leq 10$ kyrs (green), $10 < t \leq 15$ kyrs (yellow) and 15 kyrs $\leq t \leq 25$ kyrs (orange). The darker and thicker line represents the starting point of the evolution.

In Table 3.1 the maximum amplitude (m), its colatitude (deg) and its rate of dis-

placement (mm/yr) were displayed. In this case, the evolution varies from 0 to 19 kyrs, as after this instant the forebulge is completely submerged.

t (kyrs)	colatitude (deg)	amplitude (m)	rate (mm/yr)
0	13.0	22.48	0.43
1	13.0	23.41	1.25
2	12.9	24.78	1.41
3	12.8	26.11	1.28
4	12.8	27.23	0.95
5	12.7	28.05	0.63
6	12.6	28.19	0.30
7	12.5	28.63	-0.03
8	12.5	28.40	-0.43
9	12.4	27.86	-0.71
10	12.3	27.01	-1.49
11	12.3	24.75	-2.84
12	12.2	21.63	-3.35
13	12.2	18.17	-3.51
14	12.2	14.68	-3.46
15	12.2	11.29	-3.30
16	12.3	8.10	-3.06
17	12.3	5.17	-2.81
18	12.4	2.49	-2.53
19	12.4	0.08	-2.28

Table 3.1: Temporal evolution of the peak from 0 kyrs to 19 kyrs.In this table, the peak's colatitude (deg), its amplitude (m) and its rate of displacement (mm/yr) is displayed.

This data confirmed the qualitative description explained previously and enriched it with further details:

1. The peak of the forebulge reached a maximum amplitude of 28.6 m. This value is relative to the surface of this Earth Model, which is a sphere of radius r = 6371 km;

2. firstly, the peak migrated from 13.0° to 12.2° colatitude; then, the direction of motion reversed and migrated from 12.2° to 12.4° colatitude before going below 0 m;

3. at t = 13 kyrs the peak was subjected to its maximum rate of subsidence, which was -3.5 mm/yr;

4. today, the peak subsides with a velocity of -3.3 mm/yr.

3.2 Current Land Subsidence and Rising Sea Level

In Table 3.2 the minimum rate of radial displacement, its colatitude and the corresponding radial displacements were displayed. The evolution varies from t = 15 kyrs to t = 15.2 kyrs. First of all, from Table 3.2 it is possible to establish that glacial isostasy alone

t (kyrs)	colatitude (deg)	minimum rate (mm/yr)	amplitude (m)
15.00	12.0	-3.3164	11.04
15.05	12.0	-3.3074	10.87
15.10	12.0	-3.2983	10.71
15.15	12.0	-3.2890	10.54
15.20	12.0	-3.2796	10.38

Table 3.2: Time evolution of the minimum rate of radial displacement. In the first column, the colatitude (deg) at which the maximum rate is found is displayed. In the second column, the value of the minimum rate (mm/yr) is displayed, while in the third column the corresponding radial displacement (m) is displayed.

is not responsible for subsidence rates greater than 3.3 mm/yr. Furthermore, the variations in the maximum subsidence rate are sufficiently small to be considered constant at 3.3 mm/yr throughout this time interval. In fact, all values found in the forebulge region can be considered constant over such a short time interval. The minimum rate of radial displacement is always found at the same colatitude, which is 12°, and does not coincide with the peak of the forebulge, even though it is very close to it. Overall, the piece of land found at 12° will be subjected to 66.0 cm of vertical displacement in the next two hundred years.
In Figure 3.4 the spatial distribution of the rates of subsidence were displayed. Three main aspects emerge from the graph:

1. The subsidence region does not coincide with the forebulge, as subsidence is registered even in depressed land;

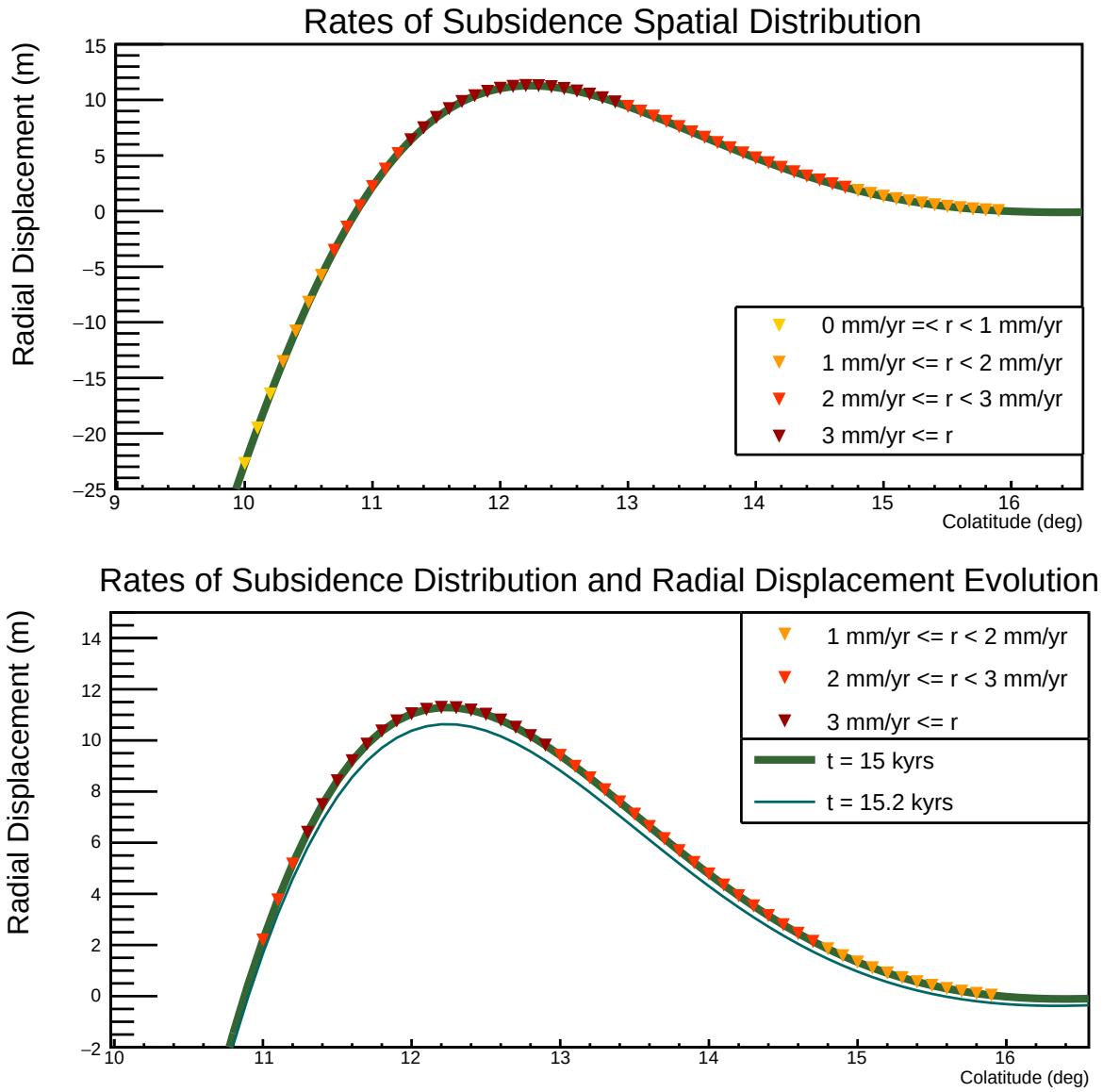

Figure 3.4: In the first graph, the rates of subsidence of the whole subsidence region are displayed. In the second one, the rates of subidence are focused on the forebulge region; furthermore, the green, thick line represents the radial displacements at t = 15 kyrs, while the thin blue line represent the radial displacements at t = 15.2 kyrs. The subsidence rates indicated in the legend are taken with their absolute values.

2. the subsidence rates tends to be higher (in absolute value) where the radial displacements themselves are higher;

3. the spatial distribution of the rates of radial displacement is not symmetric: at the same value of radial displacement, the computed rate of radial displacement at the left of the peak is higher (in absolute value) then at the right.

In particular, the third point lead to further investigations on the reasons behind the outward motion of the forebulge's peak for t $>$ 15 kyrs, shown in Table 3.1. In fact, by computing the horizontal displacements at t = 15 kyrs and at t = 16 kyrs, it was possible to verify that in both cases they are still negative, which implies a general inward movement. Therefore, this apparent paradox can be explained by assuming that at least at the beginning the outward motion is in fact apparent and due to the fact that the left part of the forebulge collapses faster than the right one [Brandes et al., 2025].
Finally, by comparing the maximum rate of subsidence (changed in sign, so as to obtain the corresponding rising in sea level) with PSMSL annual trend, it is possible to establish that TABOO predictions overestimate the contribution of post glacial isostasy to Rising Sea Level. In fact, in New York area the vertical land movement related to post glacial isostasy should be (2.90 ± 0.12) mm/yr $- (1.3 \pm 0.7)$ mm/yr $= (1.6 \pm 0.2)$ mm/yr, in contrast to the 3.3 mm/yr predicted by TABOO. Therefore, while TABOO can still be used to qualitatively predict the forebulge time evolution and its characteristics, both the Laurentide Ice Sheet and Earth model need to be improved in order to obtain reliable and precise predictions.

3.3 Controlling Parameters of the Forebulge

Load History

From Figure 3.5a it is possible to deduce that the removal of equilibrium at the Last Glacial Maximum has a great influence on the forebulge shape, as it produces a larger and taller upheaval, with a peak of 27 meters. On the other hand, the loading time does not seem to affect the forebulge shape significantly, while it has an important influence on the distribution of the rates of radial displacement (Figure 3.5b). However, the most realistic scenario, which corresponds to a loading time of 90 kyrs, reproduces similar results to model 0.
Then, model 0 was compared with a more realistic time history for the Laurentide Ice Sheet (Figure 3.6). These graphs are consistent with what was found in the previous investigation:

1. The number of glaciations in addition to the last deeply affects the forebulge shape, since for n = 8, the forebulge is about 27 m high;

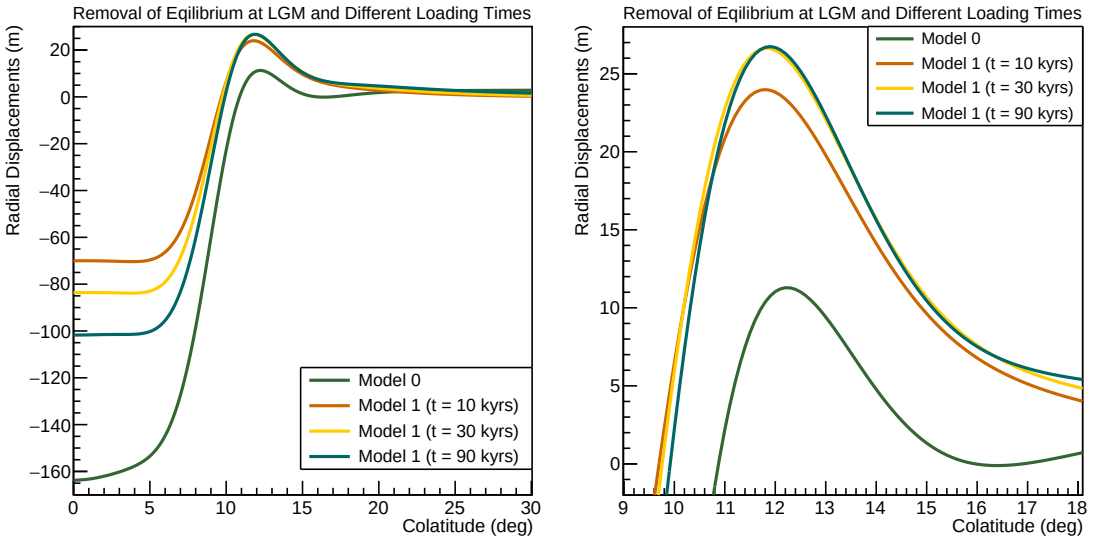

(a)

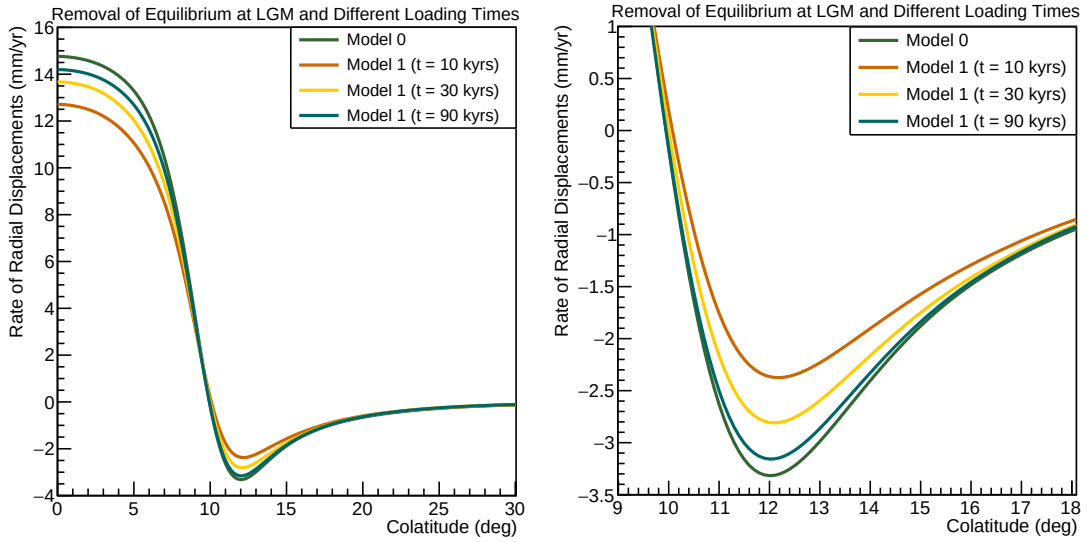

(b)

Figure 3.5: Comparison between the radial displacements (3.5a) and the corresponding rates (3.5b) at t = 15 kyrs of model 0 (green) and model 1, which uses the saw tooth load history with one glaciation in addition to the last and three three different loading times: $\tau_1 = 10$ (red) kyrs, $\tau_2 = 30$ (yellow) kyrs and $\tau_3 = 90$ kyrs (blue).

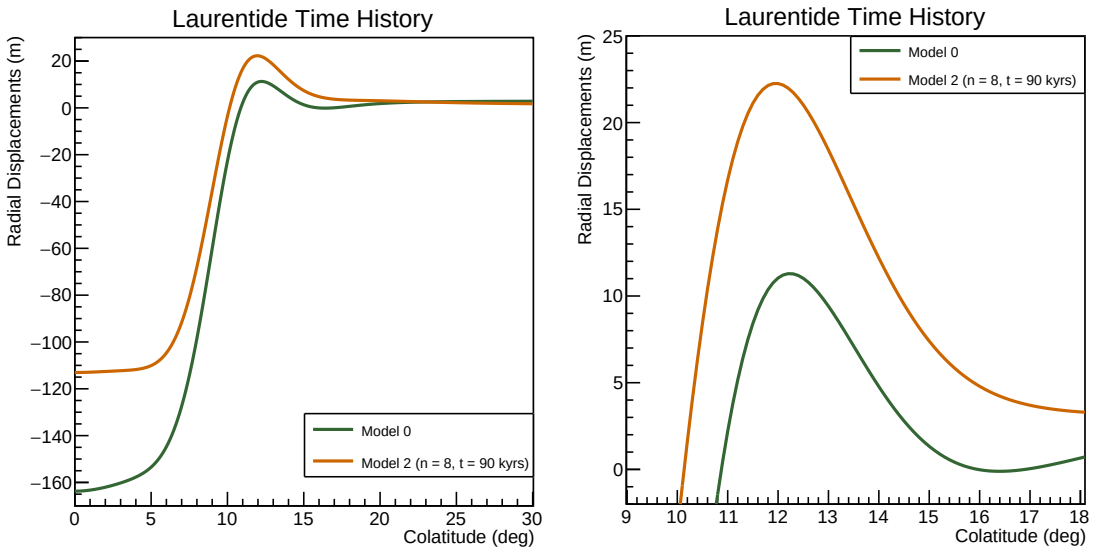

(a)

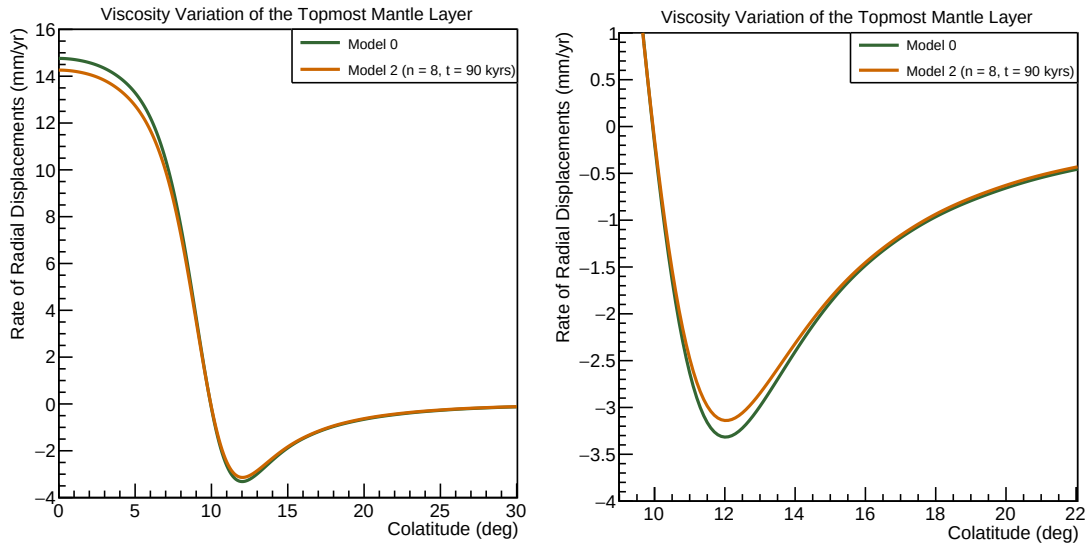

(b)

Figure 3.6: Comparison between the radial displacements (3.6a) and the corresponding rates (3.6b) at t = 15 kyrs of model 0 (green) and model 2 (red), which uses a more realistic time history for the Laurentide Ice Sheet: 9 glaciations, 90-kyrs-long loading phases and 10-kyrs-long deglaciations.

2. even though the loading time affects the distribution of rates of subsidence, for t = 90 kyrs the differences between model 0 and model 2 are negligible, which was stated by the previous graph.

Therefore, the removal of equilibrium at the Last Glacial Maximum is fundamental for determining the forebulge shape, but can be neglected when computing the subsidence rates.

Load Geometry

Figure 3.7 shows that the load geometry has a significant impact on both radial displacements and rates of radial displacement in the region that the load had covered and on what had been the edge of the load.
Concerning the radial displacements:

1. The disk load produces a less deep depression because with equal heights, the parabolic load has less mass than a disk load. As a consequence, in order to satisfy the condition of equal masses, the disk maximum height is smaller, which results in a less deep depression;

2. the depression produced by the disk load is flat, which comes from the fact that the load's height is constant at its maximum value. On the contrary, the depth of a depression induced by a parabolic load smoothly decreases as it departs from the center of the load, where it reaches its maxmimum depth;

3. the deformations computed at the edge of the disk load results form the step-edge of this kind of load, which is quite unrealistic.

However, in both cases the discrepancies in the forebulge region are trivial.
Then, a simulation was performed by varying the load amplitude. In particular, Figure 3.8 shows that the forebulges induced by a 10°-wide ice cap (model 0) and a 5°-wide one (model 4) are basically identical: the second one is just shifted to the left, accordingly to the different load amplitudes. On the contrary, there is a significant difference in the deformations induced in the depression: this is due to the fact that the maximum height for the two ice sheets is the same; therefore the load of model 4 has a steeper profile, which then affects the induced deformations.
Instead, it is more interesting to analyze the impact on the rates of radial displacement, which were shown in Figure 3.9. In this case, in addition to the discrepancies in the depression and in addition to the shift towards left, there is also a significant difference in the absolute values of rates of subsidence in the forebulge region. In particular, a narrower glacier produces smaller (in absolute value) rates of subsidence.
However, one must keep in mind that this analysis has the sole purpose of investigating

the role of the ice sheet's amplitude in determining the radial displacements and their rates, as 5° is not a realistic value for the Laurentide Ice Sheet.

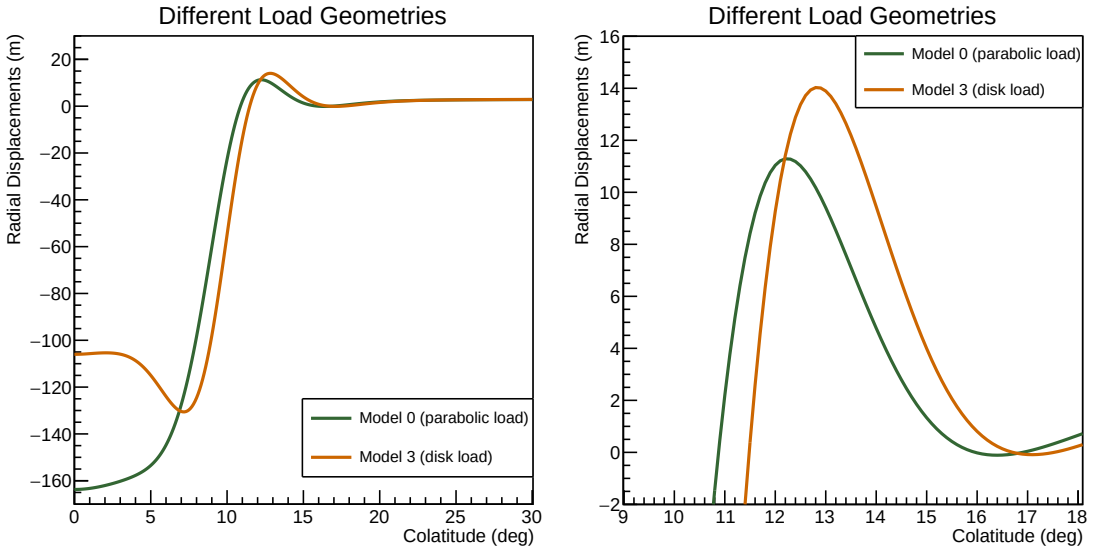

(a)

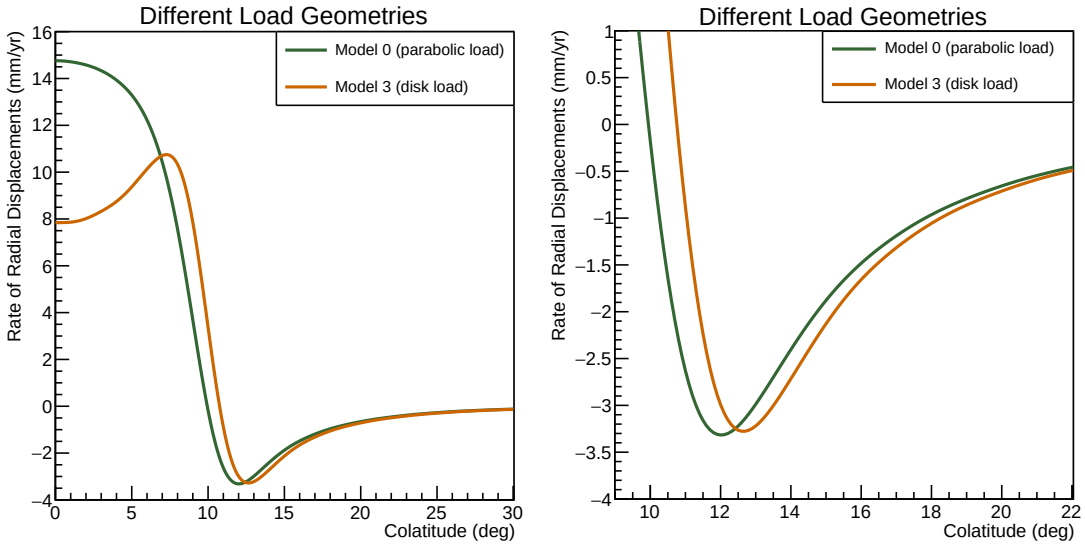

(b)

Figure 3.7: Comparison between the radial displacements (3.7a) and the corresponding rates (3.7b) at t = 15 kyrs of model 0 (green) and model 3 (red), which uses a disk load of the same mass and amplitude as model 0.

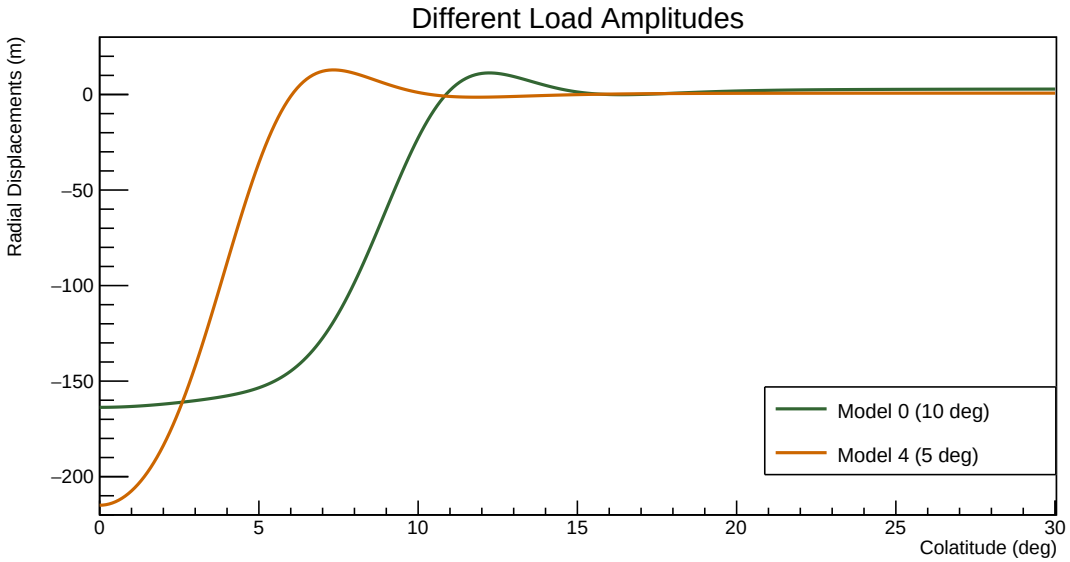

Figure 3.8: Comparison of the radial displacements induced by model 0 (green), an ice cap 10° wide, and model 4 (red), a 5°-wide one, at t = 15 kyrs.

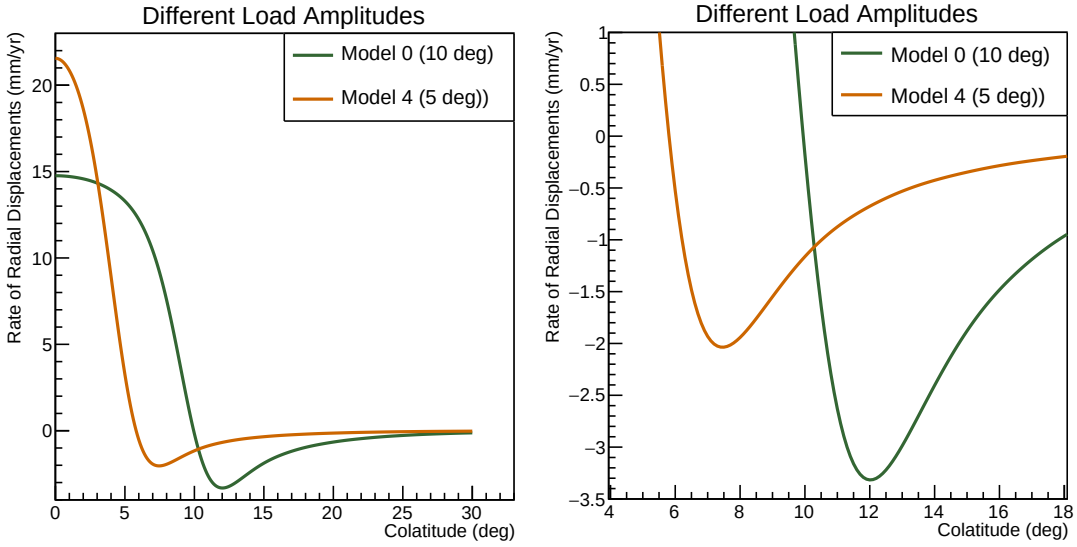

Figure 3.9: Comparison of the rate of radial displacements induced by model 0 (green), an ice cape 10° wide, and model 4 (red), a 5°-wide one, at t = 15 kyrs.

Make Model

Figure 3.10 shows the dependence of radial displacements and rates of radial displacements on the lithospheric thickness.
In particular, a thicker lithosphere is less susceptible to radial deformations, as it better balances the load. Therefore, the forebulge is shorter and farther away from the load. On the contrary, a thin lithosphere is subject to significant deformations, as the forebulge is taller and closer to the load. The rates of radial displacement vary consequently: the thicker the lithosphere, the slower the measured rates of subsidence are, and vice versa.
A similar result was found by varying the viscosity of the three mantle layers accordingly to model 6, which was explained in the Method. In particular, the higher the viscosity, the higher the deformations: this is due to the fact that more viscous the mantle layers are, the longer the deformations remain impressed in the lithosphere (and vice versa), as shown in Figure 3.11a. The same results were found by varying the topmost layer only. In particular, the radial displacements induced accordingly to the two scenarios were compared in Figure 3.11:

1. The forebulge that rises if only the topmost layer has a high viscosity (model 7) is much taller than the forebulge of model 6 (with high viscosity). This result implies that the viscosity of the upper layer influences the structure of the forebulge significantly;

2. the depression that forms when using model 6 (with high viscosity) is extremely more pronounced than the one obtained by using model 7 (with high viscosity). Thus, this allows to conclude that the viscosity of the lowest layers majorly influences the depression underneath the load.

There are no significant differences concerning model 6 and 7 with low viscosity.
In Figure 3.12, the rates of radial displacement obtained using both model 6 and 7 were shown. In particular, it is evident that the computed rates are lower than the ones foreseen by model 0 both for a higher-viscosity-model and for a lower-viscosity-one (and for both model 6 and 7). In particular, this results from two aspects:

1. If the viscosity is high, the rates at which the deformations occur is slower. This is why a high-viscosity model produces lower rates of radial displacement;

2. if the viscosity is low, the rates at which the deformations occur is faster; however, since the analysis is computed at the same instant t, the involved piece of lithosphere is closer to a configuration of equilibrium than in the case of Model 0. This is why a low-viscosity-model produces slower rates of radial displacement than model 0.

Furthermore, for both models 6 and 7, and for both the cases of low and high viscosity, the region of subsidence (negative rates of radial displacements) is interested by smaller (≈ 0) rates of subsidence.

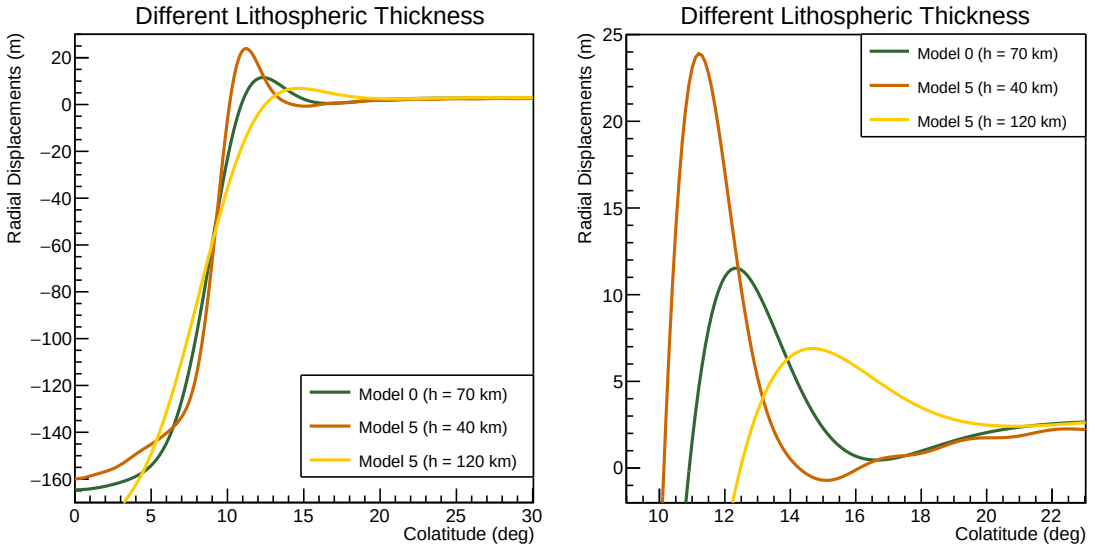

(a)

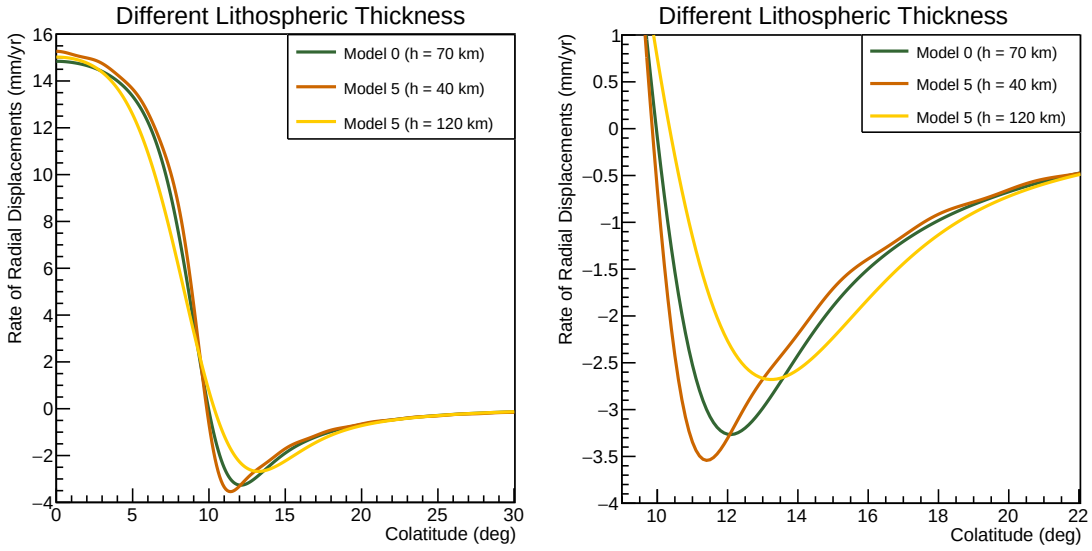

(b)

Figure 3.10: Comparison between the radial displacements (3.10a) and the corresponding rates (3.10b) of three different values for the lithospheric thickness: 70 km (green), 40 km (red) and 120 km (yellow), at t = 15 kyrs.

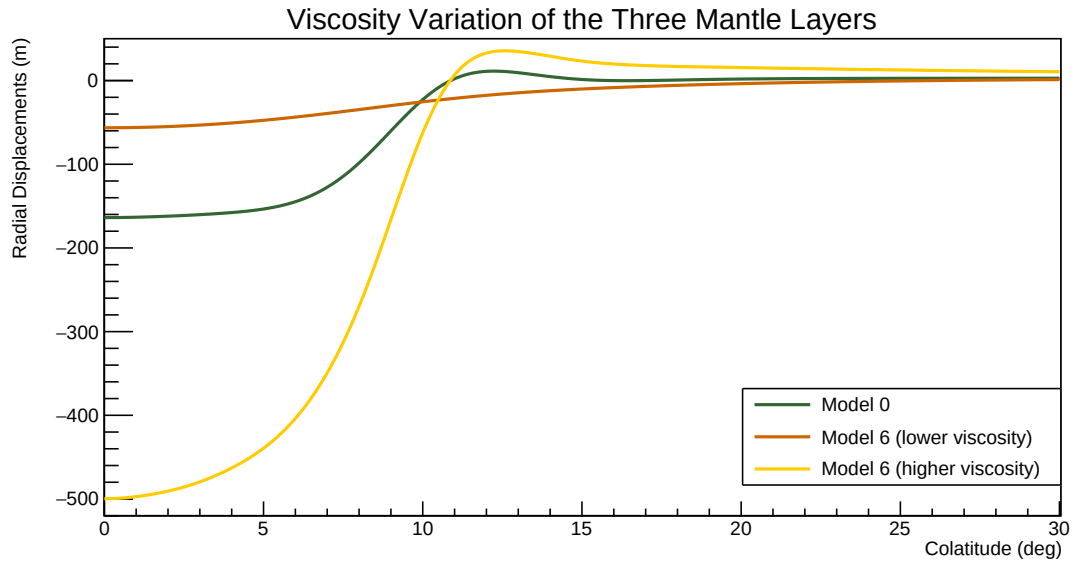

(a)

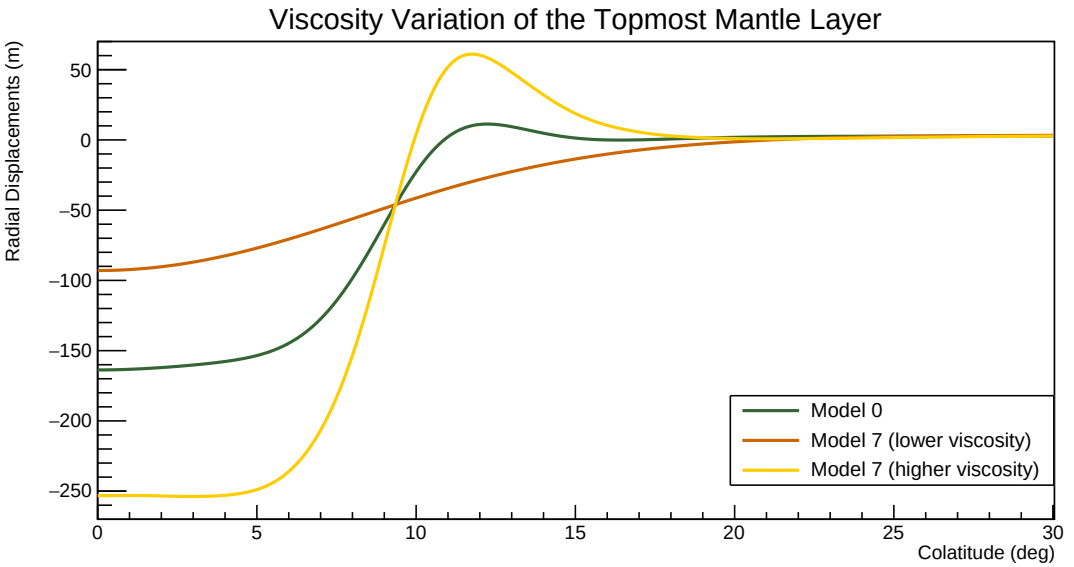

(b)

Figure 3.11: Comparison between the radial displacements induced accordingly to the two different configurations for model 6 (Figure 3.11a) and for model 7 (Figure 3.11b), at t = 15 kyrs.

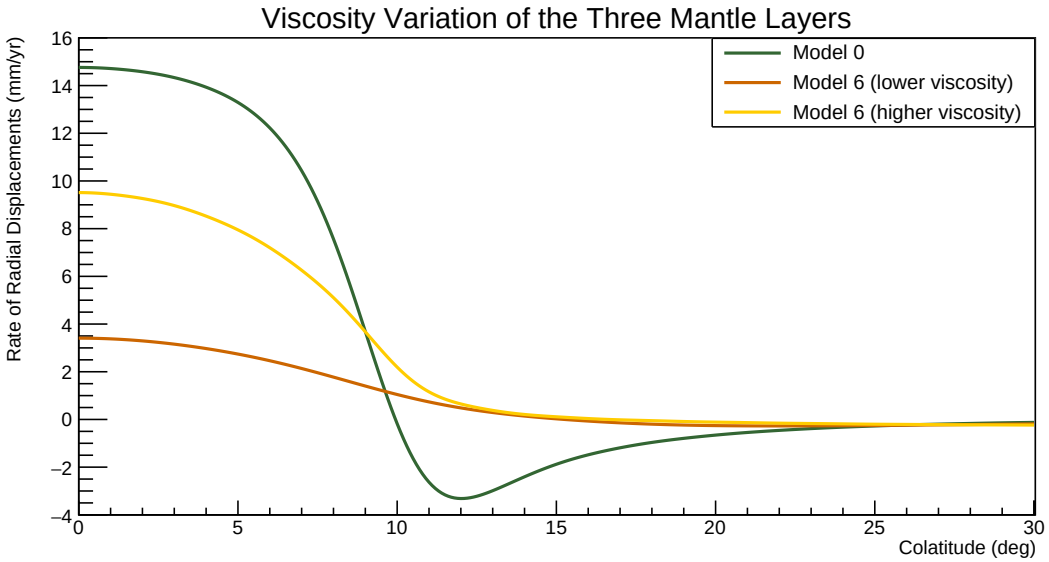

(a)

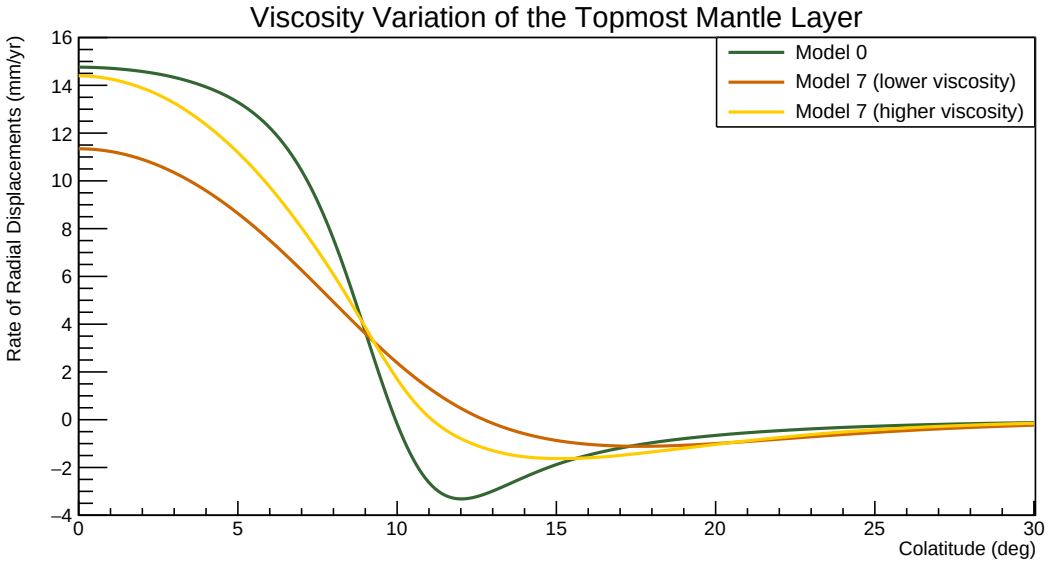

(b)

Figure 3.12: Comparison between the rates of radial displacements induced accordingly to the two different configurations for model 6 (Figure 3.12a) and for model 7 (Figure 3.12b), at t = 15 kyrs.

Conclusions

The forebulge is a dynamic structure which, during the load deglaciation, keeps moving inward and growing until it reaches its maximum amplitude (28.6 m). At this point, the forebulge starts collapsing and the rates of radial displacement change in sign, until the minimum rate of subsidence is reached (-3.5 mm/yr). This happened about two thousands years ago according to the time conventions used for this investigation. In the next thousands of years, the forebulge will continue to collapse while migrating outward. At present time, the lowest rate of subsidence in North America was predicted to be -3.3 mm/yr, and was found close to the peak of the forebulge. However, thsi value is not compatible with th current annual trend of rising sea level measured at New York The Battery station, which is known to be on the top of the LIS-related forebulge. In particular, monthly data from this station establish an annual trend of (2.90 ± 0.12) mm/yr, of which $\sim (1.3 \pm 0.7)$ mm/yr are due to climate change and ice melting. Therefore, TABOO rates overestimate the land movement due to post glacial isostasy, and both the Earth and ice model need to be improved in order to make reliable predictions. In fact, the features of the post-glacial forebulge and of subsidence rates highly depend on both the load and the Earth characteristics, and TABOO can still be used to identify these dependencies. In particular, considering the radial deformations and their rates computed at t = 15 kyrs (which, according to the time convention used for this investigation, corresponds to present time):

1. The removal of equilibrium at LGM, that is to say the addition of one or more glaciations in addition to the last, determines a taller and larger forebulge, with a peak reaching around 27 m. However, this variation does not influence the corresponding rates significantly. On the contrary, time of load formation has a greater impact on the rates of subsidence: the shorter the building time, the smaller the subsidence rate (in absolute value). However, by choosing a realistic building time like 90 kyrs, one obtains the same rates distribution as if the building time had been neglected. Therefore, the removal of equilibrium at LGM can be neglected when analyzing the subsidence rates;

2. a different geometry mainly affects the depression and the immediately adjacent region. In particilar, here a disk geometry can produce unrealistic results that can

be improved by choosing the parabolic shape, which has a less steep edge than a disk one;

3. the load half-amplitude does not influence the forebulge shape significantly. Instead, it has a more significant impact on the forebulge depression, which is deeper for narrower loads (with equal load heights), and on the subsidence rates, which are higher (in absolute values) for wider loads;

4. the lithospheric thickness has an obvious impact on the forebulge shape, as a thinner lithosphere shows a more significant flexural response to a surface load than a thicker one. Consequently, a thinner lithosphere shows higher rates of subsidence (in absolute value) than a thicker one;

5. the viscosity of the topmost mantle layer has an important impact on the forebulge shape that today is measured. In particular, the higher the viscosity, the taller and wider the forebulge measured today. The viscosity of the lower mantle layer majorly affects the depth of the depression, which is higher for higher-viscosity mantle models; on the other hand, the subsidence rates are in general lower (in absolute value) for both high and low viscosity models.

References

Backus, G. (1986). Poloidal and toroidal fields in geomagnetic field modeling. *Reviews of Geophysics*, *24*. https://doi.org/10.1029/RG024i001p00075

Brandes, C., Steffen, H., Steffen, R., Li, T., & Wu, P. (2025). Effects of the Last Quaternary Glacial Forebulge on Vertical Land Movement, Sea-Level Change, and Lithospheric Stresses. *Reviews of Geophysics*, *63*. https://doi.org/e2024RG000852

Cathles, L. M. (1975). *Viscosity of the Earth's Mantle*. Princeton University Press.

Farrel, W. E. (1972). Deformation of the Earth by Surface Loads. *Reviews of Geophysics and Space Physics*, *10*.

Gornitz, V., Couch, S., & Hartig, E. K. (2001). Impacts of sea level rise in the New York City metropolitan area. *Global and Planetary Change*, *32*. https://doi.org/S0921-8181(01)00150-3

Holgate, S. J., Matthews, A., Woodworth, P. L., Rickards, L. J., Tamisiea, M. E., Bradshaw, E., Foden, P. R., Gordon, K. M., Jevrejeva, S., & Pugh, J. (2013). New Data Systems and Products at the Permanent Service for Mean Sea Level. *Journal of Coastal Research*, *29*. https://doi.org/10.2112/JCOASTRES-D-12-00175.1

Mitrovica, J. X. (1996). Haskell [1935] revisited. *Journal of Geophysical Research: Solid Earth*, *101*. https://doi.org/https://doi.org/10.1029/95JB03208

Moreno-Parada, D., Alvarez-Solas, J., Blasco, J., Montoya, M., & Robinson, A. (2023). Simulating the Laurentide Ice Sheet of the Last Glacial Maximum. *The Cryosphere*. https://doi.org/10.5194/tc-17-2139-2023

Motoyama, H., Fujita, S., Goto-Azuma, K., Fujii, Y., & Watanabe, O. (2007). Northern Hemisphere forcing of climatic cycles in Antarctica over the past 360,000 years. *Nature*, *448*. https://doi.org/10.1038/nature06015

PSMSL. (2025a). Long Term Trends [Access Date: August 20, 2025]. https://psmsl.org/products/trends/long_term_trends.php

PSMSL. (2025b). Methods used for fitting trends [Access Date: August 20, 2025]. https://psmsl.org/products/trends/methods.php

PSMSL. (2025c). Obtaining Tide Gauge Data [Access Date: August 20, 2025]. https://psmsl.org/data/obtaining/

Sabadini, R., Piersanti, A., & Spada, G. (1995). Toroidal/poloidal partitioning of global post-seismic deformation. *Geophysical Research Letters*, *22*(8), 985–988. https://doi.org/10.1029/95GL00819

Severinghaus, J. P., & Brook, E. J. (1999). Abrupt climate change at the end of the last glacial period inferred from trapped air in polar ice. *Science*, *286*. https://doi.org/10.1126/science.286.5441.930

Spada, G., Barletta, V. R., Klemann, V., Riva, R. E. M., Martinec, Z., Gasperini, P., Lund, B., Wolf, D., Vermeersen, L. L. A., & King, M. A. (2011). A benchmark study for glacial isostatic adjustment codes. *Geophysical Journal International*, *185*. https://doi.org/10.1111/j.1365-246X.2011.04952.x

Spada, G. (2003a). TABOO user guide. https://samizdat.mines.edu/home-old/

Spada, G. (2003b). The theory behind TABOO. https://samizdat.mines.edu/home-old/

Spada, G., & Melini, D. (2025). *Glacial Isostatic Adjustment: Theory for a Spherically Symmetric Earth and Numerical Results*. Springer.

Turcotte, D. L., & Gerald, S. (2014). *Geodynamics*. Cambridge University Press.

Yuen, D. A., Sabadini, R. C. A., Gasperini, P., & Boschi, E. (1986). On transient rheology and glacial isostasy. *Journal of Geophysical Research: Solid Earth*, *91*. https://doi.org/10.1029/JB091iB11p11420

Zhao, S. (2013). Lithosphere thickness and mantle viscosity estimated from joint inversion of gps and grace-derived radial deformation and gravity rates in north america. *Geophysical Journal International*, *194*. https://doi.org/10.1093/gji/ggt212

Ringraziamenti

Infine, vorrei dedicare questo spazio a tutte le persone cui devo la realizzazione di questo elaborato e il completamento del percorso di studi.
Per primo, mi rivolgo al mio relatore, che ringrazio per avermi assegnato questo compito e per avermi seguito con attenzione per tutto l'anno accademico, prima come docente e poi come relatore.
Quindi, ringrazio i miei genitori, che mi hanno permesso di studiare senza che mi dovessi preoccupare d'altro: siamo abituati a darlo per scontato, e forse dovremmo smettere di farlo. Ringrazio mia sorella Valentina, per essere da sempre il mio punto di riferimento e miglior consigliera, e per avermi accompagnata nel viaggio più bello della mia vita, l'Islanda. Vorrei parlare anche del mio gatto Riso, che ringrazio per avermi fatto compagnia durante le lunghissime giornate di studio, e per tutte le volte in cui mi ha obbligato a fare pausa buttandomi libri e astuccio per aria. Ringrazio la nonna Nara, per essere da sempre il modello di donna che aspiro a diventare, per tutte le battute sarcastiche e per l'affetto che ogni giorno mi dimostra. Ringrazio anche la nonna Renata, per la sua infinita dolcezza, per essersi ricordata la data di ogni esame per potermi dare l'"in bocca al lupo!", e per i tortellini più buoni che io abbia mai mangiato. Infine, ringrazio il nonno Adriano, il nonno Giuseppe che mi guarda da lassù, e tutto il resto della famiglia, zii e cugini, per non avermi mai fatto sentire sola.
Quindi, ringrazio la mia migliore amica Eleonora, per parlarmi tutti i giorni, da sei anni - e anche se gli argomenti sono sempre gli stessi, con te non sono mai noiosi. Ringrazio anche Laura e Matteo: siete le persone su cui più faccio affidamento, e sono grata per la cura che dedicate a coltivare il nostro rapporto. Infine, ringrazio la mia migliore amica Valentina, per le grosse risate e per le infinite sessioni di gossip; per le serate passate a giocare ai videogiochi e per essere da sempre la persona che più mi capisce. Ele, Lau, Matte e Vale: grazie per avermi aiutata a ricordare chi fossi davvero e cosa fossi capace di fare; senza il vostro prezioso sostegno, non avrei raggiunto questo traguardo.
Ringrazio anche i miei compagni di università, per aver reso divertente ogni lezione e ogni viaggio in treno: grazie a voi, questi tre anni sono volati. Mi rivolgo in particolare a Laura e a Sebastiano, per essermi stati vicini dal primo giorno, e per avermi insegnato ad affrontare - e apprezzare - la nostra facoltà. Un grazie anche a Francesca, per la sua ospitalità e per il suo senso dell'umorismo, Bianca, per la sua spontaneità, e Riccardo, per

essere inaspettatamente profondo in qualsiasi discussione. Mi rivolgo anche a Samuele, Mattia, Silvia, Alberto e Arianna, e a chiunque abbia contribuito a rendere più leggera l'attesa prima di un esame o le interminabili giornate di lezione.
Poi, ringrazio tutti i miei amici, a cui chiedo infinitamente scusa per tutte le volte in cui ho detto "Non posso, devo studiare": rimedierò, lo prometto. In particolare, mi riferisco a Virginia, Giada, Giovanni, Stefano, Jacopo, Arianna, Giacomo e Nicolò, e a chiunque abbia contribuito a rendere una serata, o un viaggio, o una qualsiasi idea folle più divertente.
Vorrei ringraziare anche la mia professoressa di inglese del liceo, per avermi insegnato che gli unici ostacoli insormontabili sono quelli che decidiamo di non affrontare. Mi rivolgo anche a tutti gli altri professori e compagni delle superiori, nonostante io li abbia in gran parte persi di vista, perché a volte non si è grati per ciò che si riceve da una persona, ma per ciò che una persona ci permette di diventare. E io, con voi, tra i banchi del liceo, sono sbocciata.
Infine, ringrazio Federica, per la sua costanza, determinazione e senso del dovere. Perché di fronte ad ogni delusione (e ce ne sono state parecchie!), ha stretto i denti e perseverato, fino ad ottenere ottimi risultati; per aver preso ogni rifiuto e fallimento come motivo ulteriore per provare il suo valore. E non mi sarei mai scoperta così forte se non fosse stato per ogni persona che è entrata nella mia vita, facendo ordine o scompiglio: per questo motivo, ringrazio anche chi invece di aiutare ha ostacolato, e chi invece di capire ha giudicato; perché non è questione di ciò di che una persona ci toglie, ma ciò che una persona ci permette di diventare. E io, grazie a tutti voi, hamiltoniana dopo hamiltoniana, mi sono scoperta nel posto giusto.

Ad Maiora,
Federica